ADDIS ABABA UNIVERSITY

COLLEGE OF NATURAL AND COMPUTATIONAL SCIENCES

SCHOOL OF EARTH SCIENCES

ASSESSMENTS OF SEASONAL VARIABILITY OF LAND SURFACE TEMPERATURE USING MULTI-RESOLUTION SATELLITE DATA, OF THE YEAR 2021 IN CASE OF TANA SUB BASIN, NORTH WEST ETHIOPIA

A Thesis Submitted to the School of Graduate Studies of Addis Ababa University in Partial Fulfillment of the Requirements for the Degree of Masters of Science In Remote Sensing and Geo-Informatics

By
YITAYIH ADDIS ASMARE

ID: GSR/0034/12

Advisors:
K. V. Suryabhagavan (PhD)
Tibebu Kassawmar (PhD)

Addis Ababa, Ethiopia

February, 2022

ADDIS ABABA UNIVERSITY

COLLEGE OF NATURAL AND COMPUTATIONAL SCIENCES

SCHOOL OF EARTH SCIENCES

ASSESSMENTS OF SEASONAL VARIABILITY OF LAND SURFACE TEMPERATURE USING MULTI-RESOLUTION SATELLITE DATA, OF THE YEAR 2021 IN CASE OF TANA SUB BASIN, NORTH WEST ETHIOPIA

A THESIS SUBMITTED TO THE SCHOOL OF GRADUATE STUDIES OF Addis Ababa UNIVERSITY IN PARTIAL FULFILLMENT OF THE REQUIREMENTS FOR THE DEGREE OF MASTERS OF SCIENCE IN REMOTE SENSING AND GEO-INFORMATICS

By
YITAYIH ADDIS ASMARE
ID: GSR/0034/12

Addis Ababa, Ethiopia

February, 2022

Addis Ababa University

School of Graduate Studies

Thesis Approval Form

This is to certify the thesis prepared by **Yitayih Addis Asmare** entitled "***assessments of seasonal variability of Land Surface Temperature using multi-resolution satellite data, of the year 2021, the case of Tana Sub Basin, north west Ethiopia***" is submitted in partial fulfillment of the requirements for the Degree of Master of Science in Remote Sensing and Geo-informatics compiles with the regulations of the university and meets the accepted standards to originality and quality.

Yitayih Addis		15/03/22
Candidate	Signature	Date

Signed by the Examining Committee:

Dr. K.V. Suryabhagavan		29/03/2022
Adviser	Signature	Date
Dr. Tibebu Kassawmar		/ /
Co-Adviser	Signature	Date
Dr. Binyam Tesfaw		15/03/2022
Examiner	Signature	Date
Dr. Behailu Berehanu		15/03/2022
Examiner	Signature	Date
Dr. K.V. Suryabhagavan		29/03/2022
Chairman	Signature	Date
Dr. Balemwal Atnafu		04/04/2022
Head, Department of Earth Sciences	Signature	Date

DECLARATION

I hereby declare that the dissertation entitled **"*assessments of seasonal variability of Land Surface Temperature using multi-resolution satellite data, of the year 2021, the case of Tana Sub Basin, North West Ethiopia*"** has been carried out by me under the supervision of **Dr. K. V. Suryabhagavan and Dr. Tibebu Kassawmar**, School of Earth Sciences, Addis Ababa University, Addis Ababa during the year 2019−2022 as a part of Master of Science programme in Remote sensing and Geo-informatics. I further declare that this work has not been submitted to any other University or Institution for the award of any degree or diploma.

Addis Ababa, Ethiopia

Date: March, 2022

Yitayih Addis

Assessments of seasonal variability of Land surface temperature using Multi-resolution Satellite data, in case of Tana Sub-basin, North West Ethiopia

Name: Yitayih Addis Asmare, MSc Thesis
Addis Ababa University, February 2022

Abstract

Quantifying Land Surface Temperature (LST) has a great role for biophysical and landscape monitoring like that of hydrology, urban management and environment. LST is a fundamental physical property relevant to many hydrological and atmospheric processes. The objective of this study is to assess the Spatial inter-seasonal variability of LST using Multi-resolution satellite Data of dry and wet (rainy) season of the year 2021 in the case of Tana Sub Basin, North West Ethiopia. Split Window Algorithm (SW) was used to retrieve LST, Mann-Kendall trend test for inter season trend analysis and the Pearson correlation coefficient (r) for correlation analysis. In this study, LST from three satellite images was retrieved and downloaded to see the Spatial and inter-seasonal LST variation. The maximum LST was gained from Sentinel-3 in April with LST 51°C, whereas the minimum LST was 5°C from Landsat 8 during February of the dry season. Similarly, the maximum LST in wet (rainy) season was extracted from Landsat 8 in June with LST 42°C and the minimum was in Sentinel-3 in July with 8°C. Spatially the maximum LST was observed in the periphery of the study area. The minimum LST was observed in central parts of the study area, this is due to Lake Tana. The relationship between LST obtained from Landsat 8, MODIS, and Sentinel-3 and mean temperature shows strong values of r >= 0.5 in dry and wet (rainy) season, except July of Sentinel-3. The correlation result shows a better fit between temperature and LST results obtained from Landsat 8 followed by MODIS in dry season. Similarly, Landsat 8 has a better correlation followed by MODIS in wet (rainy). In general, LST retrieved from Landsat 8 thermal bands shows better than the other two. From Mann-Kendall trend test for both Landsat 8 and MODIS LST there was statistically insignificant increasing, whereas for Sentinel-3 no trend in dry season. While, in wet (rainy) season the Mann-Kendall trend tests for both Landsat 8 and MODIS LST, there was a statistically insignificant decreasing trend. In contrast Sentinel-3 mean LST revealed statistically insignificant decreasing trend. The study result showed that, satellite based LST retrieval is time and cost effective. Therefore, it is recommended to be used with caution.

Keywords: LST, SCA, Seasonal variability, SWA

Acknowledgments

First and foremost, praised be to **"Almighty GOD"** for making it possible and for providing me with the fortitude and patience to give me to complete my study.

I wish to express my deepest gratitude to my advisors Dr. K.V.Suryabhagavan and Dr. Tibebu Kassawmar for their, generous support, fruitful comments, feedback, and continuous guidance throughout the thesis process and made this study possible.

I also thank Dr. Balemwal Atnafu, Head School of Earth Sciences Addis Ababa University for frequently writing letters of support for data providers; and for letting us access Remote Sensing and GIS Lab facilities.

I want to thank the Ethiopian Civil Service University for sponsoring my study. I also would like thank to Centeral Statistical Agency of Ethiopia and National Metrological Agency (NMA) for providing the shapefile of administrative data and historical meteorological data.

I am greatly indebted to Haylemikael Hans, Neway Kifle, Alemu Yetwale and all my Remote Sensing and Geo-Informatics stream classmates for their contribution of ideas and encouragement during the study and this research work.

Finally, I would like to thank all my family members for their helpful nature throughout my study.

Table of contents

List of Figures

List of Tables

List of acronyms

AATSR	Advanced Along Track Scanning Radiometer
ACZ	Agro Climatic Zone
ArcGIS	Aeronautical Reconnaissance Coverage Geographic Information System
ASTER	Advanced Space-borne Thermal Emission and Reflection Radiometer
AL	Radiance additive scaling factor
AVHRR	Advanced Very High-Resolution Radiometer
BRDF	Bidirectional reflectance distribution function
BT	Brightness Temperature
CSA	Central Statistical Agency
CWVC	Atmospheric Column Water Vapor Content
DEM	Digital Elevation Model
DNs	Digital Numbers
DOS	Dark Object Subtraction
EOS	Earth Observing System
ERDAS	Earth Resource Data Analysis System
ESA	European Space Agency
ESRI	Environmental Systems Research Institute
ETM	Enhanced Thematic Mapper
ETM+	Enhanced Thematic Mapper Plus
GeoTIFF	Geostationary Earth Orbit Tagged Image File Format
HDF	Hierarchical Data Format
ITCZ	Inter-Tropical Convergence Zone
K	Kelvin
LDCM	Landsat Data Continuity Mission
LSE	Land Surface Emissivity
LST	Land Surface Temperature
MK	Mann Kendall
MODIS	Moderate Resolution Imaging Spectro-radiometer
ML	multiplicative scaling factor

MWA	Mono-Window Algorithm
MSS	Multispectral Scanner System
NASA	National Aeronautics and Space Administration
NDVI	Normalized Difference Vegetation Index
NIR	Near Infrared
NMA	National Meteorological Agency
NOAA	National Oceanic and Atmospheric Administration
OLI /TIRS/	Operational Land Imager/ Thermal Infrared Sensor
OLCI	Ocean and Land Color Instrument
POWER	Prediction of Worldwide Energy Resources
QGIS	Quantum Geographic Information System
RBT	Radiances and Brightness Temperatures
RS and GIS	Remote Sensing and Geographic Information System
RTE	Radiative Transfer Equation
SC	Single-Channel
SCP	Semi-automatic Classification Plugin
SST	Sea Surface Temperature
SLSTR	Sea and Land Surface Temperature Radiometer
SNAP	Sentinel Application Platform
SWA	Split Window Algorithm
SWIR	Short Wave Infrared
T_{air}	Surface Air Temper
TIR	Thermal Infrared
T_{skin}	Surface Skin Temperature
TM	Thematic Mapper
TOA	Top of Atmosphere
USGS	United States Geological Survey
UTM	Universal Transverse Mercator

CHAPTER ONE

1 Introduction

1.1 Background

Land surface temperature (LST) is a key parameter in land surface process physics on local and universal scales, a combination of all results from the land surface and energy flows between the surface and atmosphere and has been utilized as a fundamental element in surface energy balance modeling (Alkhaier et al. 2012; Bateni et al. 2013; Hain and Anderson, 2017; Yoo et al. 2020).

Temperature changes rapidly based on time and place; thus, factors that interact with LST include soil moisture, air temperature, and evapotranspiration (Meng et al., 2009; Srivastava et al., 2013; Yoo et al., 2018, 2020). Hence, it seems necessary to be aware of spatial air temperature changes on wide scales to conduct climate, drought, air pollution, and the urban heat island effect are just a few examples of socio-environmental challenges with LST (Albright et al. 2011; Park et al. 2020; Yoo et al. 2019, 2020b; Ziaul and Pal, 2018).

Under clear sky conditions, thermal infrared (TIR) sensors are a primary source for producing satellite-based LSTs. A Moderate Resolution Imaging Spectroradiometer is found in several polar-orbiting TIR sensors. The advanced space-borne thermal emission and reflection radiometer in space (Abrams et al., 2002; Yoo et al., 2020). LST is a vital determinant that influences long-wave radiation exchange between the surface and atmosphere. Algorithms for calculating land surface temperature using split-window radiances have progressed to the point where accuracies of 1-3 K are possible. Even though cooling differentials can occur, better accuracies (closer to 1K) are observed at night when differential surface heating is absent (Sensor et al., 2017).

Only surface-leaving radiation collected by satellite sensors can be used to calculate Land Surface Temperature (LST) and emissivity over vast areas (*LST_LSE_Review_IJRS_2002*, n.d.). At national to international scales, LST is a critical determinant in determining energy and water budge (Anderson et al., 2008; Karnieli et al., 2010; Khorchani et al., 2018; Kustas and Anderson, 2009; Li et al., 2013; Zhang et al., 2008). Remotely sensed observations of

land surface temperature (LST) are acknowledged as one of the core messaging of the urban thermal environment (Jin, 2012; Voogt and Oke, 2003; Weng, 2009).

Satellite thermal infrared sensors currently available give the data with varying spatial resolution and temporal coverage that can be used to estimate land surface temperature. In several spectral channels, satellite sensors measure the surface-leaving radiance influenced by the atmosphere; the corresponding brightness temperatures are computed by reversing Planck's function. Various climate and environmental models have used satellite-based land surface temperature (LST) as one of the primary parameters (Yoo and Park, 2020). Thermal remote sensing is widely acknowledged as a valuable source of quantitative and qualitative information on land surface processes, as well as a tool for characterizing, analyzing, and modeling land surface information (Quattrochi and Luvall, 1999, 2004; Sobrino et al. 2009).

1.2 Statement of the problem

Surface skin temperature observations (T_{skin}) obtained via satellite remote sensing provide useful climatological information with high spatial resolution and global coverage, complementing traditional ground observations of surface air temperature (T_{air}) and revealing new information about land surface characteristics. Due to the complicated characteristics of environmental variables such as vegetation cover, topography, soil texture, and land cover patterns, as well as the seasonal influence, which are all strongly associated with LST, LST has a very large variation in both the spatial and temporal domains. Although in-situ ground measurements give an accurate surface temperature at a specific site, they do not provide spatially continuous LST data across large areas. Satellite remote sensing has proven to be a feasible option for spatiotemporal LST characterization on a regional to global scale. Globally averaged temperatures have increased as a result of global warming (M. Jin and Dickinson, 2002). To retrieve LST, different satellites were put into space at different times of the year. Satellites like Landsat, MODIS, and, more recently, Sentinel and ASTER are in orbit and play this function.

For TM/ETM+ sensors, the previous Landsat series used a single thermal band in the atmospheric window between 10 and 12 micrometers, and SC was used to retrieve the LST. However, the Landsat-8 TIRS differs from earlier sensors in that it divides a single thermal

band into two TIR bands. For the retrieval of surface temperature, previous LST methods used the single-channel (SC) approach, which is entirely limited to a single thermal band. However, because the bandwidths of TIRS bands are shorter than those of the previous TM/ETM+TIR band, the SC algorithm may produce problems using TIRS sensors (Solanky et al., 2018). A new mathematical structure of the split-window (SW) algorithm was proposed to solve this problem, in which two TIR bands were used instead of a single TIR band. In this paper acquiring LST from Landsat 8, MODIS and sentinel-3 an SW algorithm has been used. In-situ measurement has good accuracy but it is limited in space and time. So retrieving LST from the satellite is the best practice in terms of space and time effectiveness. But here the researcher is trying to know which satellite is good for retrieving LST when compared with temperature data in different seasons.

1.3 Objectives of the study

1.3.1 General objective

To assess the seasonal variability of Land Surface Temperature Multi-resolution Satellite data dry and wet season of the year 2021 in the case of Tana Sub Basin, North West Ethiopia.

1.3.2 Specific objectives

- To map land surface temperature in January, February, March and April (dry season) and June, July and August (rainy season) of the year 2021 using Landsat 8 TIRs, MODIS and Sentinel-3.
- To assess the Spatial and inter-seasonal variability of LST
- To compare the LST results obtained from Landsat 8, MODIS, and Sentinel-3 against mean near surface air temperature data.

1.4 Research questions

This study has the following research questions:

- What is the land surface temperature of the study area in January, February March, April, June, July and August of the year 2021 from Landsat 8, MODIS and Sentinel-3?

- What are the Spatial and inter-seasonal variations in LST?
- Which sensor LST result has a strong correlation with mean near surface air temperature data?

1.5 The scope of the study

The scope of this study is spatially limited only to Tana Sub Basin in the northwest, Ethiopia. Temporally its extent is in assessments of inter-seasonal variability of Land Surface Temperature Using Landsat 8, MODIS and Sentinel-3 data for only January, February, March and April (dry season) and June, July and August (wet season) the year 2021 of the sub-basin. This study didn't include May, September, October November and December of the year 2021 and focused on only day time LST in all sensors.

1.6 Significance of the study

The result of this research shows multi-sensor based retrieved LST map and different accuracy levels when it compared with mean near surface air temperature data, hence it is collected in some stations compared with it and having the most fitted or accurate LST can have a great role for anyone who wants to retrieve LST from satellite imageries like that of environmentalist, urban planners, agricultural expertise, hydrologist and such like. Moreover, this research has a more role by being a baseline for further researchers who aspire to do research in connection with it.

1.7 Organization of the thesis

This thesis is arranged into six chapters. The first chapter states the introduction, statement of the problem, objectives of the study, research questions, scope, and significance of the study. The literature review was organized under chapter two. Description of the study area, material and methods that were used is manipulated in chapter three. In chapter four, the results were analyzed, but it was discussed in chapter five in detail. Chapter six presents the conclusion and recommendations.

CHAPTER TWO

2. Literature Review

2.1. Land surface temperature

Different authors defined LST in different ways: for example (Reddy and Manikiam, 2017) It is defined as the surface temperature that can be measured when the ground surface comes into direct contact with the measurement device. The skin temperature of the land surface is referred to as LST. On the other hand (Solanky et al., 2018) defined it as the temperature of the earth's surface as seen through the atmosphere by a remote sensing satellite; the surface being whatever it observes when looking through the atmosphere to the ground.

LST is an important physical characteristic in land surface processes that have to do with surface-atmosphere interactions and energy balance(Wan, 1999, Jiménez-Muñoz et al., 2008). LST values change over time and space, and analyzing their variation can reveal previously unknown processes. This is important for a variety of applications, including vegetation monitoring, climate change, environmental studies, geothermal monitoring, and thermal studies of volcanic sites, among others (Flynn et al., 2001; Li et al., 2013; Q. Qin et al., 2011). External factors such as solar radiation, vegetation, soil, and terrain characteristics can all affect LST measurements (Li et al., 2013; Q. Qin et al., 2011). Over the years, there has been an increase in interest in thermal-infrared (TIR) remote sensing and LST retrieval, and several strategies for retrieving LST have been described (Jiménez-Muñoz et al., 2008). As a result, a variety of LST retrieval algorithms have been devised, ranging from single-channel to multi-channel methods. Although, due to the corrections of both atmospheric and emissivity effects to acquire precise readings, LST retrieval from space is still considered to be complex and challenging (Li et al. 2013). The radiative transfer equation (RTE) is the relationship between TIR data derived from satellites and LST.

2.2. Near-surface air temperature

Thermodynamic temperature (or, equivalently, kinetic temperature) has traditionally been measured with in situ thermometers in a shelter with good thermal contact with the air at 1.5–2 m. This is the temperature of the surface air, or, more precisely, the temperature of the air at shelter height. T_{skin} is connected with this near-surface air temperature, but it can vary

depending on the land cover or sky conditions; changes can be significant, for example, in sparsely vegetated places where sensible heat flux balances by the net radiation.

2.3. Advantage of retrieving land surface temperature

Land surface temperature (LST) has been identified as one of the most important elements in the physical processes of surface energy and water balance at local to global scales by the Remote Sensing community during the last several decades (Brunsell and Gillies, 2003; Zhang et al. 2008;Karnieli et al. 2010; Kustas and Anderson, 2009; Solanky et al. 2018;). Evapotranspiration, climate change, hydrological cycle, vegetation monitoring, urban climate and environmental studies are only a few of the applications for LST (Bastiaanssen et al., 1998; Kogan, 2001; Su, 2002; Arnfield, 2003; Voogt and Oke, 2003; Weng et al. 2004; Kalma et al. 2008; Weng, 2009; Hansen et al. 2010; Reddy and Manikiam, 2017; Solanky et al. 2018;).

2.4. Thermal remote sensing technologies

Thermal remote sensing is recognized to be a major source of quantitative and qualitative information on land surface processes and for their characterization, analysis, and modeling (Jiménez-Muñoz et al. 2008; Quattrochi and Luvall, 1999, 2004). Electromagnetic energy having a wavelength of 3 to 20 micrometers is referred to as thermal infrared radiation. The 3 to 5 and 8 to 14-micrometer ranges are used in most remote sensing applications (due to absorption bands). The major distinction between thermal infrared and near-infrared is that thermal infrared is energy that is emitted, whereas near-infrared is energy that is reflected, comparable to visible light.

2.4.1. Landsat

The most well-known satellites are the Landsat, which has the longest track record of earth observations from space. The visible resolution of the Landsat 4 and 5 Thematic Mapper (TM) was 30 meters, and the TIR resolution was 120 meters (band 6, 10.4–12.5 meters). Although the Enhanced Thematic Mapper (ETM+) on Landsat 7 captures thermal data at a resolution of 60 meters (including band 6, 10.4–12.5 meters), Landsat 4 and 5 are no longer collecting data. Landsat 7 has a 16-day revisit period and a near-polar Sun-synchronous orbit, which implies that it will scan a given location on Earth at around the same local time.

The number of studies has increased in recent years as the Landsat data repository has only been available for free since 2008. Landsat data has the drawback of not being collected at night and having limited thermal calibration (Tomlinson et al. 2011). The Landsat-8 satellite (also known as the Landsat Data Continuity Mission, LDCM) was launched in February 2013 to provide continuity of remote sensing data acquired at high spatial resolution by instruments on previous Landsat satellites such as the multispectral scanner system (MSS), the thematic mapper (TM), and the enhanced thematic mapper plus (ETM+).

According to Irons et al. (2012); Solanky et al. (2018) Landsat-8 is equipped with an operational land imager (OLI) as well as a thermal infrared sensor (TIRS). OLI uses eight bands in the visible, near-infrared, and shortwave infrared portions of the electromagnetic spectrum, as well as a panchromatic band with a 15 m spatial resolution, to record data with a 30 m spatial resolution. The TIRS sensor measures TIR radiation in the atmospheric window between 10 and 12 m with a spatial resolution of 100 m and two bands (bands 10 and 11). More specifications are presented in Table 2.1.

Table 2.1 Specification of Landsat bands (Vlassova and Pérez Cabello, 2016).

Satellite and sensor	Band	Spectral range in μm	Spatial resolution (m)
Landsat-5 TM	3 (Red)	0.63 - 0.69	30
	4 (NIR)	0.76 - 0.90	30
	7 (SWIR 2)	2.064 - 2.345	30
	6 (Thermal IR)	10.40 - 12.50	120
Landsat-7 ETM+	3 (Red)	0.63 - 0.69	30
	4 (NIR)	0.76 - 0.90	30
	7 (SWIR 2)	2.064 - 2.345	30
	6 (Thermal IR)	10.40 - 12.50	60
Landsat-8 OLI	4 (Red)	0.64 - 0.67	30
	5 (NIR)	0.85 - 0.88	30
Landsat-8 TIRS	10 (Thermal IR)	10.60 - 11.19	100
	11(Thermal IR)	11.50 -12.51	

2.4.2. MODIS

Moderate Resolution Imaging Spectroradiometer (MODIS) is a sensor onboard the Terra and Aqua platforms that provides information about the Earth's surface in 36 wavebands, including visible, near-infrared, shortwave infrared (SWIR), and thermal wavelengths. The MODIS sensor collects data in 36 spectral channels, including thermal infrared channels 20,

22, 23, 29, 31, and 32, which are centered on 3.79, 3.97, 4.06, 8.55, 11.03, and 12.02 mm (Hulley et al., 2012). Because of its worldwide coverage, radiometric resolution, and dynamic range for a variety of land cover types, MODIS is particularly valuable for the LST output. It offers great calibration accuracy in several thermal infrared bands that are used to retrieve SST (Sea Surface Temperature), LST (Land Surface Temperature), and atmospheric characteristics (Wan, 1999). LSTs are calculated using a split-window technique. The emissivity in MODIS bands 31 and 32 is calculated using thermal infrared BRDF models based on land-cover types(Snyder et al., 1998; Snyder and Wan, 1998). The day/night LST approach extracts land-surface temperature and band emissivity simultaneously from daytime and overnights MODIS data in seven TIR bands using pairings of daytime and nighttime MODIS data. The NASA Warehouse Inventory Search Tool was used to download LST composites from the Land Processes Distributed Active Archive Center (LPDAAC) website https://ladsweb.modaps.eosdis.nasa.gov/. The data is in HDF-EOS format and is projected using the Sinusoidal Projection System (Center, n.d.). The data was sub-set to the study area and re-projected from Sinusoidal projection to UTM Zone 37 N projection system with WGS84 datum at the same time. ArcGIS was used to convert the data from HDF-EOS to GeoTIFF format. After that, GIS capabilities in ArcGIS software were used to evaluate the various data layers in GeoTIFF format.

The MODIS 1 km LST is calculated using a generalized split-window (GSW) method based on brightness temperature measurements taken at MODIS bands 31 (10.78-11.28 m) and 32 (11.77-12.27 m) (Wan and Dozier, 1996; Yoo et al., 2020). The collection 6 MOD11A2 LSTs are tile-based global products that provide per-pixel temperature and emissivity values, with a resolution of 1 km and an accuracy of approximately 1 K (Wan, 2014; Duan et al., 2017).

2.4.3. Sentinel

Characteristics of sentinel-3 are shown in (Table 2.2).

Table 2. 2 Characteristics of Sentinel-3 (Sentinel.esa.int, n.d.)

Instrument	SLSTR
Processing Level	Level-1B
Spatial Resolution	1 km
Temporal Resolution	Daily
Collection:	OLCI and SLSTR ESA-Copernicus-Sentinel-3 A and B Level 1 (ArchiveSet 450)

Land surface temperature (LST) is an important indicator of the global ecological environment and climate change. The Sea and Land Surface Temperature Radiometer (SLSTR) onboard the recently launched Sentinel-3 satellites provide high-quality observations for estimating global LST (Yang et al., 2020).

Level-0, Level-1, and Level-2 are the three processing levels available in SLSTR data products, with Level-1 and Level-2 being publicly available. For nadir and oblique views, Level-1 deliverables include calibrated radiances and brightness temperatures (RBT) for each channel at the instrument grid, as well as some supplementary data. Among others, Level-2 products include sea surface temperature (SST), LST and fire radiative power (Team, 2013). As a result, estimate LSTs from SLSTR using the nadir view SLSTR Level-1B products acquired between January 2017 and December 2018. The Level-1 RBT product provides TOA brightness temperature (BT) for S7–S9 (3.74–12μm) and TOA radiances for S1–S6 (0.56–2.25μm), as well as associated Sun zenith and azimuth angles, satellite zenith and azimuth angles, and land surface elevation, among other things. These datasets are provided in Net CDF format and were downloaded from the Copernicus Open Access Hub (Copernicus, n.d.). The SLSTR LST is a Level-2 official product with a spatial resolution of 1 km. It gives LST estimations as well as several associated characteristics, such as LST, NDVI, vegetation type (biome), CWVC (atmospheric column water vapor concentration), and parameters linked to LST retrieval. The official SLSTR LST product is estimated with the following SWA, which makes implicit use of LSE Equation(1) (Remedios and Emsley, 2012).

$$Ts = af,\mathrm{i},\mathrm{pw} + \mathrm{bf},\mathrm{i}(\mathrm{T11} - \mathrm{T12})1/\cos(\theta/m) + (\mathrm{bf},\mathrm{i} + \mathrm{cf},\mathrm{i})\mathrm{T12}$$

(1)

where Ts is LST in K; a, b, and c are coefficients; T11 and T12 are the BTs in S8 and S9, respectively; subscript f corresponds to vegetation fraction; i denotes vegetation type; pw is the CWVC; θ is the satellite zenith view angle; and m is a variable depending on θ (Yang et al., 2020).

2.5. Land surface temperature retrieving algorithms

Before the emergence of earth observation satellites, determining an area's LST was challenging (EOS). It was often created for a specific set of sample points before being interpolated into isotherms to transform point data to area data. Thermal data from remotely sensed data, on the other hand, is increasingly being used to predict LST (Rajeshwari and Mani, 2014; Solanky et al., 2018). Many studies have been conducted in the past to estimate LST from satellite-derived TIR data, utilizing various approaches and methods Many methods of LST estimate have been devised and accepted in the literature; some of the most generally used approaches are split-window (SW) and Single channel (SC) algorithm. The majority of the investigations were conducted in metropolitan areas and dry and semi-arid locations, with single thermal bands being employed in several of them. LST products are routinely generated from moderate-resolution satellite data (e.g., the moderate resolution imaging spectro-radiometer (MODIS) on NASA's Terra and Aqua platforms, and the Advanced Along-Track Scanning Radiometer on the European Space Agency's Environmental Satellite) because they show the surface energy that is a function of time (Norman and Becker, 1995; Solanky et al., 2018).

Since thermal satellite data became available, researchers have experimented with a variety of methods. For the estimation of LST, the results of a recent review of existing algorithms are provided in (Tang and Li, 2013; Vlassova and Pérez Cabello, 2016) updates and complement earlier surveys (Dash et al., 2002; Li et al., 2013; Prata et al., 1995; Vlassova and Pérez Cabello, 2016). Single-channel and multi-channel algorithms are the most often employed algorithms, and they all require an a priori knowledge of surface emissivity. Some approaches employ tactics that aren't as well-known as the ones already described (e.g.

(Becker and Li, 1990; Sun and Pinker, 2003; Vlassova and Pérez Cabello, 2016). The method chosen in each case is determined by the availability and qualities of photos and supplementary data, as well as the needed quality of the results (Vlassova and Pérez Cabello, 2016). Several methods for estimating LST from a single band have been successful. A direct inversion of the Radiative Transfer Equation (RTE) and the mono-window approaches are two regularly utilized procedures (Z. Qin et al., 2001) and a single-channel algorithm (Jiménez-Muñoz and Sobrino, 2003; Vlassova and Pérez Cabello, 2016). Many retrieval techniques have exploited the idea of effective emissivity at the pixel level since the land surface has heterogeneous emissivity (Prata et al. 1995; Schmugge et al. 1998).

2.5.1. Single channel method (SCM)

Planck's law can be used to obtain LST by inverting RTE directly. In this situation, characteristics describing atmospheric conditions at the time of satellite overhead must be known, which can be derived from atmospheric profiles and radiative transfer codes (models). This information can be obtained using an online web tool designed and implemented by (Barsi et al. 2003; Vlassova and Pérez Cabello, 2016). The other two methods often used for LST retrieval from the unique thermal band are ETR approximations which avoid dependence on actual atmospheric profiles. The mono-window technique(Qin et al. 2001; Vlassova and Pérez Cabello, 2016) involves the derivation of two empirical coefficients based on atmospheric water content and near-surface air temperature, while single-channel method (Jiménez-Muñoz and Sobrino, 2003; Vlassova and Pérez Cabello, 2016) requires only knowledge of atmospheric water content to compute three atmospheric functions. When the water vapor level in the atmosphere is between 0.4 g/cm^2 and 2.5 g/cm^2, both algorithms are capable of generating LST with errors close to 1 K for the clear-sky image.

2.5.2. Split window algorithm (SWA)

The multi-channel method also known as the split-window algorithm uses radiances in two thermal bands with different atmospheric absorption to estimate the effect of the atmosphere on

the signal. The technique was first proposed by (Vlassova and Pérez Cabello, 2016) it was applied for estimating the surface temperature of sea/ocean (e.g., (Njoku et al. 1985;

Vlassova and Pérez Cabello, 2016). The method is based on the fact that atmospheric attenuation of the signal is proportional to the difference of the radiances simultaneously measured in two thermal channels. Algorithm adapted for LST estimation by (Coll et al. 1994; Vlassova and Pérez Cabello, 2016) along with atmospheric attenuation due to water vapor absorption, also estimates the effect of much greater heterogeneity of land surface emissivity on LST. The errors reported by researchers who applied the split-window method for LST estimation from several multi- and hyper spectral sensors are ~1 K (Tang and Li, 2013; Vlassova and Pérez Cabello, 2016).

CHAPTER THREE

3. Materials and methods

3.1. Study area description

The Lake Tana sub-basin is located in northwestern Ethiopia; geographically it is situated between 1210686 −1410750 m latitude, and 252986−417240 m longitude (Fig 3.1). It is found in the Amhara area of Ethiopia's highlands in the northwest. The basin's lowest point is 2916 meters above sea level, while its highest point is 4100 m. The highest point in the basin is the Simien Mountains, which are located in the north-eastern region of the basin. At 1732 m above sea level, the lake exit into the Blue Nile. The Abbay (Blue Nile River) sub-basin, which includes Lake Tana, comprises an estimated area of 15,031 km^2. The region's climate is tropical highland monsoon, with one rainy season running from June to September. The air temperature has a high diurnal but small seasonal variability with a yearly average of 20°C. The movement of the inter-tropical convergence zone (ITCZ) to the north controls the distribution of rainfall in the region (Wubneh Belete et al. 2017).

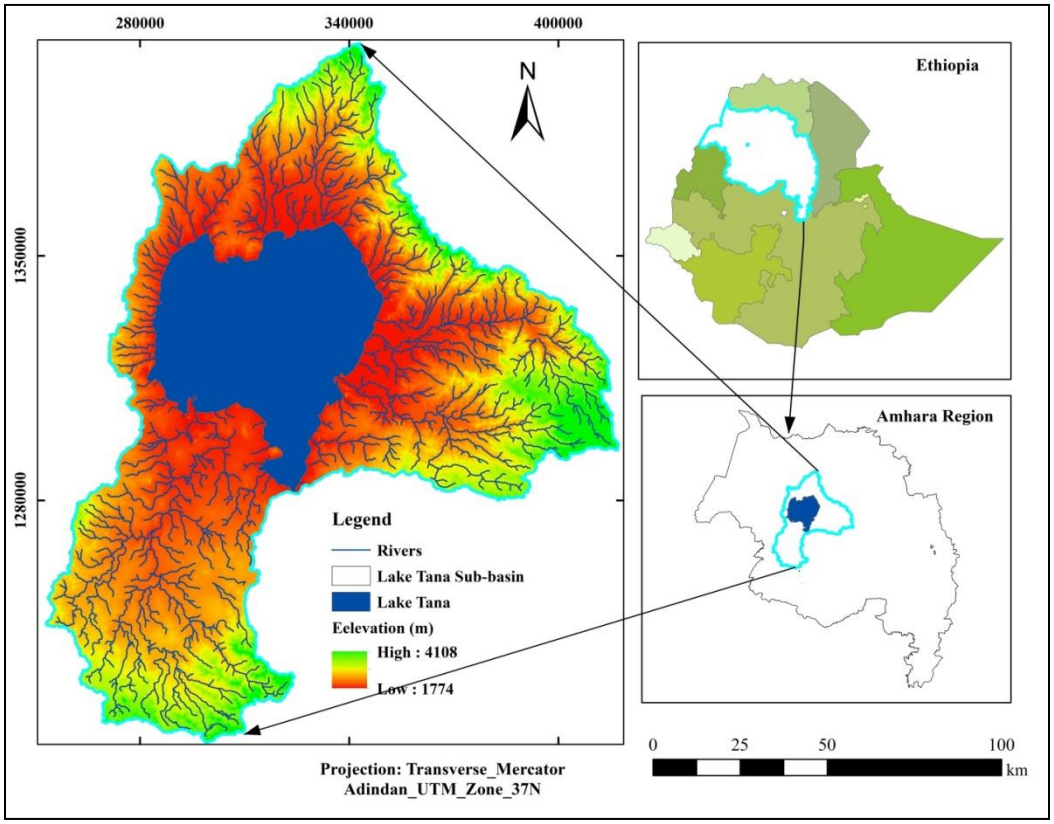

Figure 3. 1 Location map of the study area

3.1.1. Topography

The area has a maximum height of 4108 m and a minimum elevation of 1774 m. Highly elevated areas are found in the northeast and south periphery of the study area where as the lowest elevated areas are found in Lake Tana and its surrounding (Fig 3.2) shows the topography of the study area.

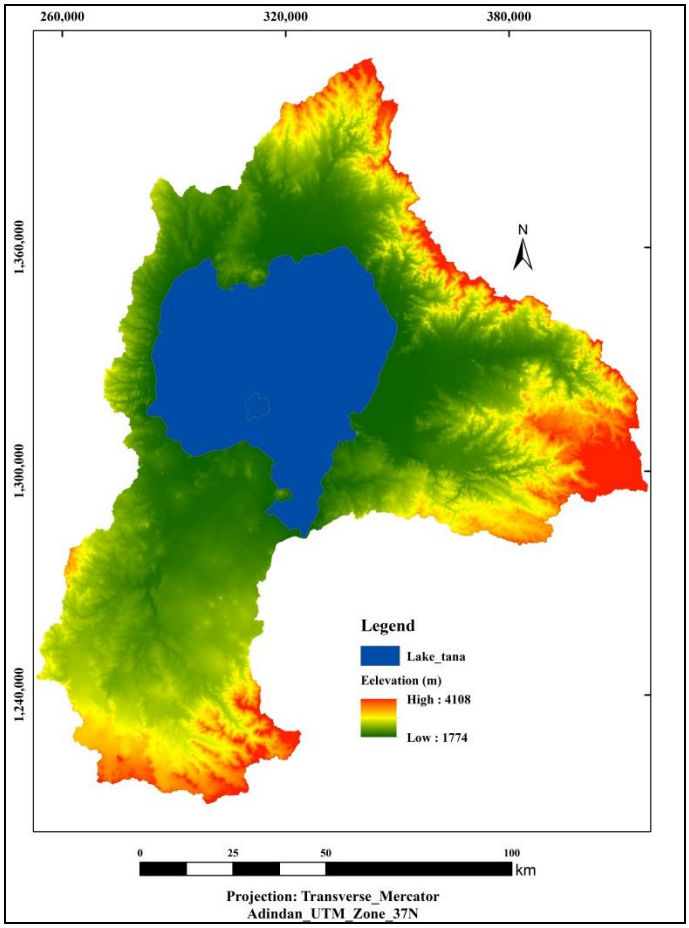

Figure 3. 2. Elevation map.

3.1.2. Temperature

The average maximum temperature from the year 1986 to 2019 of the area was observed in Gonder station at 25.72°C (Fig 3.3). The average minimum temperature from the year 1986 to 2019 was observed in Dangila with 8.65°C (Fig 3.3.).

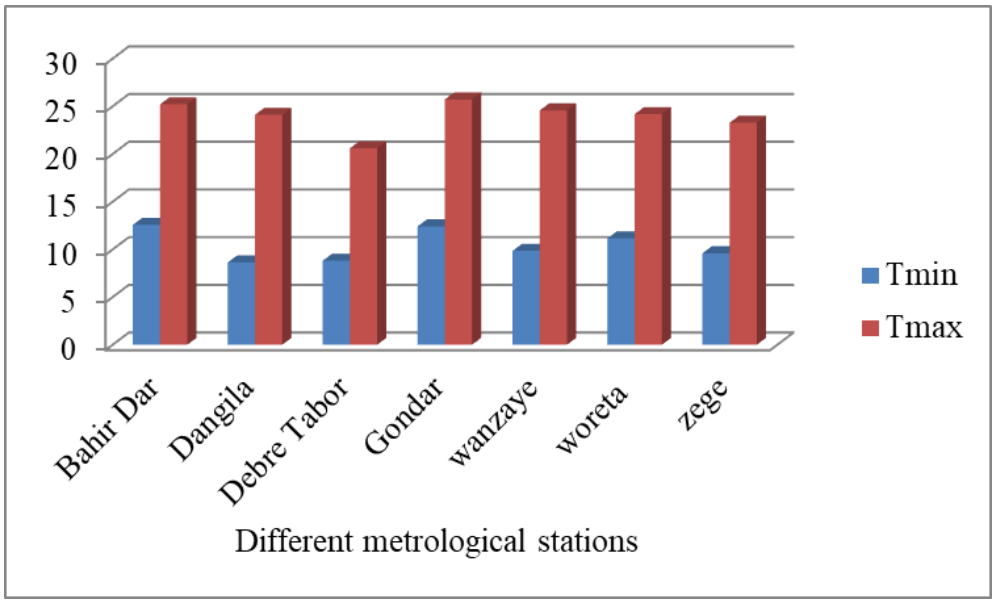

Figure 3. 3 Maximum and minimum temperature

3.1.3. Drainage

The lake receives water from more than 40 tributary rivers in the Lake Tana sub-basin. Gilgel Abay from the south, Ribb and Gumara from the east, and Megech from the North are the principal rivers that feed the lake. These four rivers, which come from the north, account for more than 93 percent of the sub basin's flow (Setegn Shimelis et al. 2008). In the meanwhile, no major rivers are flowing from the west. On the other side of the lake, the Gilgel Abay River flows 159.05 km from Sekela in the south of the basin to reach Lake Tana, covering a drainage area of 3824.88 km^2. The Gumara and Ribb rivers, which flow 103.99 km and 117.45 km, respectively to reach Lake Tana and cover a drainage area of 1476.34 km^2, are another prominent river in the Lake Tana sub-basin. The drainage of the study area is shown (Fig 3.4).

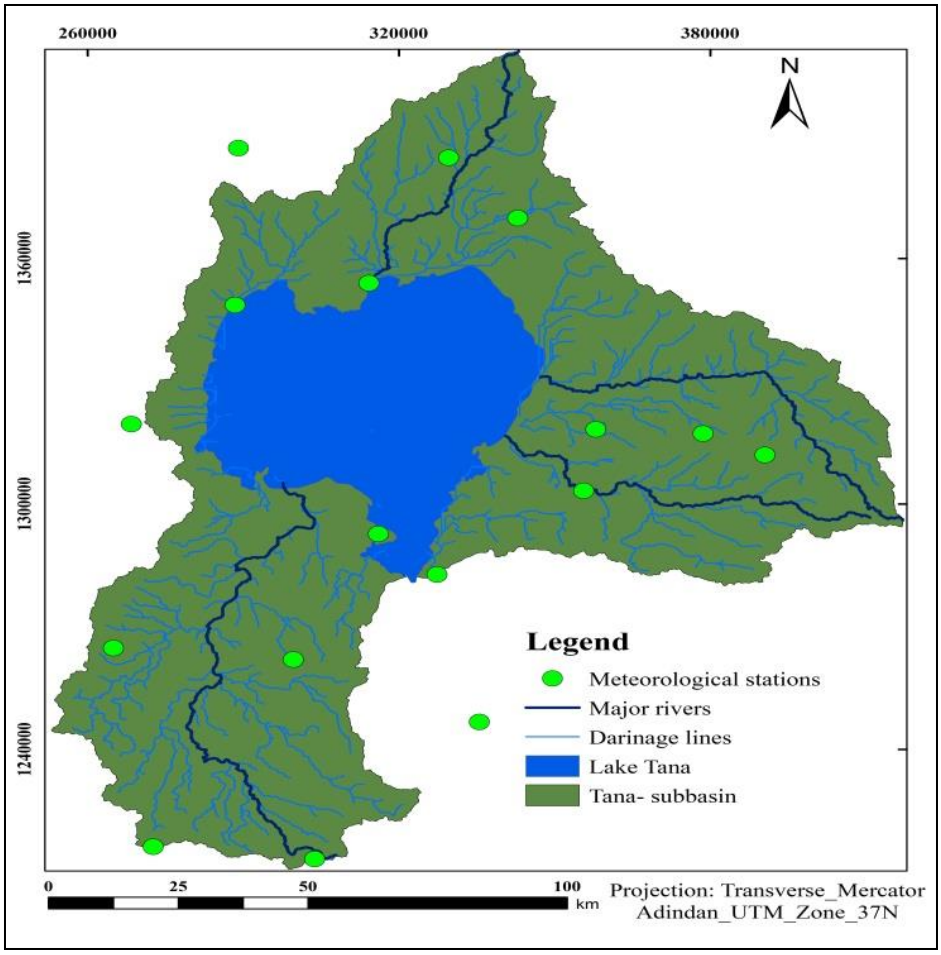

Figure 3. 4 Drainage map

.

3.2. Materials and Software

3.2.1. Materials

Primary data

The primary data used in this study were Landsat 8 OLI/TIRS, Sentinel-3 and MODIS. The MODIS LST data products (MOD11A2) Version 6 eight-day and Sentinel-3 /SLSTR/ LST product daily 1km spatial resolution imagery were publicly downloaded from the Earth Data Institute's website, Copernicus open access hub and Landsat 8 from USGS (Table 3.1). Near surface Air Temperature data for correlation were downloaded from NASA POWER Access climate (*Power Data-Access-Viewer*, n.d.).

Table 3. 1 Primary data used.

Data	Band	Spatial Resolution	Temporal resolution	Acquisition date	Purpose	Source
Landsat 8OLI/ TIRS	Band 4(red) Band5(Near-infrared)	30×30 m	16 days	2021-01-19, 2021-01-28, 2021-02-13, 2021-03-17, 2021-04-02, 2021-07-14, 2021-08-08, 2021-08-15	NDVI and LST retrieval	https://earthexplorer.usgs.gov/
	Band 10 Thermal Band11 Thermal	100 m				
MODIS	bands 31 and 32	1000 m	8 day	January ,February, March, April, June, July and August/2021	LST Product	https://ladsweb.modaps.eosdis.nasa.gov/
Sentinel-3	bands S7 - S9	1000 m	1 day	,January February, March, April, July and August/2021	LST Product	https://scihub.copernicus.eu/
DEM	-	12.5 m	-	-	To prepare elevation map	https://earthdata.nasa.gov/eosdis/daacs/asf

Secondary data

Shapefile of administrative boundary, road, and river features provided from Central Statistical Agency of Ethiopia (CSA). Other sources of secondary data include; meteorological stations temperature data from the National Meteorological Agency (NMA) of Ethiopia.

Software

ESRI's ArcGIS 10.4 and ERDAS Imagine 2015, SNAP Desktop5.0, QGIS 3.10, and Microsoft Office (Microsoft Office, Publisher, Excel and xlstat) were the main software packages used in this study.

3.3. Methods

3.3.1. Imagery preprocessing

Radiometric calibration and atmospheric correction are done for Landsat 8 OLI red (band 4) near-infrared (band 5) and TIRS thermal infrared (bands 10 (10.60 to 11.19 m) and 11 (11.50 to 12.51 m) images. In radiometric calibration, dark object subtraction is employed to convert the Digital Number (DN) obtained by remote sensors into at-atmosphere radiance images. Layer stacking, mosaicking and subseting had been conducted for Landsat 8 thermal bands of 10 and 11 and of OLI red (band4) and near-infrared (band 5). In this study, a layer stack was used for only OLI red and near-infrared bands.

3.3.2. Land surface emissivity estimation

LSE determines the absorbed quantity of heat by the object. The NDVI thresholds approach, which is a pixel-level emissivity calculation method (Equation 4), is used to calculate LSE. This method was first used to analyze data from the Advanced Very High-Resolution Radiometer (AVHRR) (Sobrino and Raissouni, 2000), and was later compared to other methods and adapted to other sensors. Using the NDVI threshold technique, the extremely linear relationship between NDVI and specific surface emissivity was utilized to compute surface-specific emissivity. The study area is divided into three categories based on the spatial resolution of remote sensing images: water bodies, natural surfaces, and urban surfaces (Liu et al., 2012; Yin et al., 2020) .

(Valor and Caselles, 1996; Yin et al., 2020) suggested a theoretical model connecting emissivity to NDVI. When the NDVI is less than 0.1, the pixel is considered bare soil with no vegetation coverage and surface emissivity of 0.96; when the NDVI is greater than 0.72, the pixel is considered vegetation with 1 vegetation coverage and surface emissivity of 0.985; and when the NDVI is between 0.1 and 0.72, the pixel is considered a spectrally mixed pixel.

The LSE of the TIR channel is calculated using three linear functions that correspond to complete vegetation, full soil, and mixed soil/vegetation content in a pixel. Because the area is covered by soil and plant, emissivity is determined using equation (4) in this study. For LSE retrieval Normalized Difference Vegetation Indices (NDVI) were calculated from OLI red and near-infrared bands using equation (2).

$$NDVI = Red - NIR/Red + NIR \quad (2)$$

The proportion of vegetation is estimated using the equation below (Anandababu et al., 2018).

$$PV = (NDVI - NDVImin/NDVImax + NDVImin)^2 \quad (3)$$

Where NDVI

$NDVI_{min}$

$NDVI_{max}$

After all land surface emissivity of study area for band 10 and band 11 were carried out (Jiménez-Muñoz et al., 2014; Yosef mengistu Darge et al., 2019).

$$\varepsilon\lambda = \varepsilon v P v + \varepsilon s(1 - Pv) + C\lambda \quad (4)$$

Where ελ land surface emissivity of band λ

ε_v- vegetation emissivity

ε_s- Soil emissivity

Pv-proportional vegetation

Cλ- cavity effect for bands 10 and 11.

$$C\lambda = (1 - \varepsilon s) \times \varepsilon v F'(1 - Pv) \quad (5)$$

Where F' geometrical factor ranging between 0 and 1 depending on the geometric distribution of the surface. Since F' cannot be estimated from remotely sensed data, (Sobrino

and Raissouni, 2000; Yosef Mengistu Darge et al., 2019) suggest using a mean value of 0.55 and some emissivity constants for Landsat 8 thermal bands presented in (Table 3.2).

Table 3. 2: Emissivity constants for band 10 and 11.

Bands	Es	Ev
Band 10	0.971	0.987
Band 11	0.977	0.989

3.3.3. Land surface temperature retrieval (SWA)

The temperature of the earth's surface that we feel when we touch or contact it is known as Land Surface Temperature (LST). Particularly it's the surface's skin temperature. The radiance multiplicative scaling factor (ML) and radiance additive scaling factor (AL) are obtained from the Metadata of the full image of band 10 and band 11 to compute the spectral radiance. The Semi-automatic categorization plugin (SCP) in QGIS was used to apply an atmospheric adjustment to the thermal bands of Landsat 8 TIRS (band 10) using the Dark Object Subtraction- (DOS-1) approach proposed by (Chavez Jr, 1988; Filgueiras et al., 2019).

Conversions of DNs to at sensor spectral radiance

The initial step in obtaining LST is to convert row digital numbers (DNs) values to sensor radiance. To convert DNs to radiance units for Landsat 8 TIRS of band10 and 11 equation 6 was used (Landsat-missions, n.d.).

$$L\lambda = ML * Qcal + AL \quad (6)$$

where Lλ is TOA spectral radiance (Watts/(m^2 *srad *μm)), ML is Band-specific multiplicative rescaling factor from the metadata (RADIANCE_MULT_BAND_x, where x is the band number),AL is Band-specific additive rescaling factor from the metadata (RADIANCE_ADD_BAND_x, where x is the band number), Qcal is Quantized and calibrated standard product pixel values (DN). This research used a few constants from metadata of the Landsat 8 TIRs (Table 3.3).

Table 3. 3. Constants collected from image meta data.

Constants	K1	K2	ML	AL
Band 10	774.8853	1321.0789	0.00033420	0.1
Band 11	480.8883	1201.1442	0.00033420	0.1

Top of atmosphere brightness temperature

Thermal band data can be converted from spectral radiance to the top of atmosphere brightness temperature using the thermal constants in the MTL file (Landsat-missions, n.d.).

$$T = K2/\ln(\frac{K1}{L\lambda} + 1) \quad (7)$$

Where:

T = Top of atmosphere brightness temperature (K)
L_λ =TOA spectral radiance (Watts/(m2 * srad * μm))
K_1 =Band-specific thermal conversion constant from the metadata (K1_CONSTANT_BAND_x, where x is the thermal band number)
K_2 =Band-specific thermal conversion constant from the metadata (K2_CONSTANT_BAND_x, where x is the thermal band number)

Land Surface Temperature Estimation

The split window Algorithm was commonly used for sentinel-3 (SLSTR), MODIS (MOD11A2) and Landsat 8 to estimate LST (Table 3.4).

$LST = Ti + c1\ (Ti - Tj)\ + C2\ (Ti - Tj)\ + C0 + \ (C3 + C4W)\ (1 - \varepsilon)\ + \ (C5 + C6W)\ \Delta\varepsilon$ (8) (Jiménez-Muñoz et al., 2014,Yosef Mengistu Darge et al., 2019) .

Where Ts is LST in Kelvin, Ti and Tj are the at-sensor brightness temperatures in the SW bands 10 and 11, E is the mean emissivity, E = 0.5 (εi + εj), Δε is the emissivity difference, Δε = (εi – εj). W is the total atmospheric water vapor content (4.12 g/cm^2).

Table 3. 4 Constants to calculate LST (Jiménez-Muñoz et al., 2014; Yosef Mengistu Darge et al., 2019).

Constant	C0	C1	C2	C3	C4	C5	C6
Value	-0.268	1.378	0.183	54.3	-2.238	-129.2	-16.4

In the case of MODIS and Sentinel-3 ESA provided the LST products for SLSTR. The split-window approach was used to create these products, which operates similarly to the LST retrieval method for Advanced Along Track Scanning Radiometer (AATSR) images (Hu et al., 2019; Schneider et al., n.d.). MODIS LST was downloaded from the Earth Data website. First geometrical corrections for both MODIS and Sentinel-3 were applied

(Reproject) and the downloaded LST were downscaled by downscaling factors 0.02 and 0.1 of MODIS and Sentinel-3, respectively. Then, clipped by study area. For both MODIS and sentinel-3 LST of January, February, March, April, June, July and August average values were taken using a raster calculator in ArcGIS. Finally, unit conversion from degree kelvin to degree Celsius took place.

$$LST(°C) = (PV \times 0.02) - 273.15 \quad (10)$$

$$LST(°C) = (PV \times 0.1) - 273.15 \quad (11)$$

Where, PV - Pixel value.

3.3.4 Spatial inter-seasonal variability of LST

To find out seasonal patterns, different statistical test methods are applied, which are classed as parametric and non-parametric tests. Parametric tests are more powerful, but they need data to be independent and properly distributed, which LST time series data rarely are. Data must be independent for non-parametric tests, but outliers are tolerated better. The Mann-Kendall (MK) test is the most popular and commonly used method for analyzing seasonal LST time-series patterns (Negash et al., 2013; Ahmad et al., 2015; Alemayehu et al., 2017; Tesfay et al., 2018; Worku et al., 2019; Abebe Arega and Arega Bazezew,2020; Samson et al., 2021). Before analyzing the MK trend, all of the data was verified to see if autocorrelation was present. As a result, there is no autocorrelation between the datasets. Sen's slope method was used to calculate the magnitude of the slope in a data time series. The null hypothesis (H0) in the Mann-Kendall test was that there was no trend in land surface temperature over two seasons of months, while the alternate hypothesis (H1) was that there was a trend (increasing or decreasing) over two seasons of months. The following are the mathematical equations for computing MK Statistics: The MK statistic (S) is calculated in the following way:

$$S = \sum_{i=1}^{n-1} \sum_{j=i+1}^{n} Sig(yj - yi) \quad (12)$$

The trend test is performed on a time series yi that is ranked from i = 1,2,3,... n – 1 and a time series yj that is ranked from j = i + 1, i + 2, i + 3,... n. Each of the data points yj is used as a reference point and the others of the data point's yi are compared to it, so that

$$Sign(\text{yj} - \text{yi}) \begin{cases} 1, if(yj - yi) > 0 \\ 0, if(yj - yi) = 0 \\ -1, if(yj - yi) < 0 \end{cases} \quad (13)$$

The sequential data values are yj and yi, and the length of the data set is n. Sen's slop non-parametric method is used to determine the true slope of an existing trend, such as the amount of change every month. Sen's technique can be utilized in situations where a linear trend can be assumed, such as:

$$f(t) = Q(t) + B \quad (14)$$

The slope is Q, and the constant is B. As a result, the Sen Slope estimator is calculated in the following way:

$$B1 = Median\{(yj - yi)|(yj - yi)\} \quad (15)$$

Computing the slope for all pairs of data that were used to compute S in Eq. for all j > i and i = 1, 2... n-1 and j = 2, 3..., n; in other words, calculating the slope for all pairs of data that were used to compute S in Eq (9). The Sen slope estimator is the median of the slopes (Rahman, A and Begum, M 2006; Samson et al., 2021)

3.3.5. Correlations of LST with mean near surface air temperature data

The linear relationship between two or more variables (land surface temperature and near surface air temperature) is described by a correlation analysis. A Pearson correlation coefficient is a numerical statistic that illustrates how two variables are related. Linear correlations between LST and near surface air temperature by a positive and negative correlation trend as linear regression (C. Li et al., 2018; Samson Tsegaye Mekasha et al., 2021). To correlate the LST obtained from remote sensing with mean temperature Pearson correlation coefficient(r) was used. The Pearson correlation coefficient results were interpreted as a strong correlation ranging from ±0.50 to 1, medium correlation ranging from ±0.30 to 0.49, and weak correlation ranging from ±0.30 to 0 (Neway Kifle and Binyam Tesfaw, 2021). The following empirical relationship was used to determine the Pearson correlation coefficient value (r):

$$r_{xy} = \sum_{i=1}^{n}(xi - \dot{x})(yi - \dot{y}) / \sqrt{\sum_{i=1}^{n}(xi - \dot{x})^2 \sum_{i=1}^{n}(yi - \dot{y})^2}$$

(16)

The obtained LST from MODIS Landsat 8 and Sentinel-3 were compared with mean Temperature data that have been downloaded from the NASA POWER Access climate website. Pearson correlations between LST and mean Temperature were performed to know how those retrieved and downloaded LST related with mean Temperature data that have been downloaded from the NASA POWER Access climate website. The overall methods are shown in (Fig 3.5).

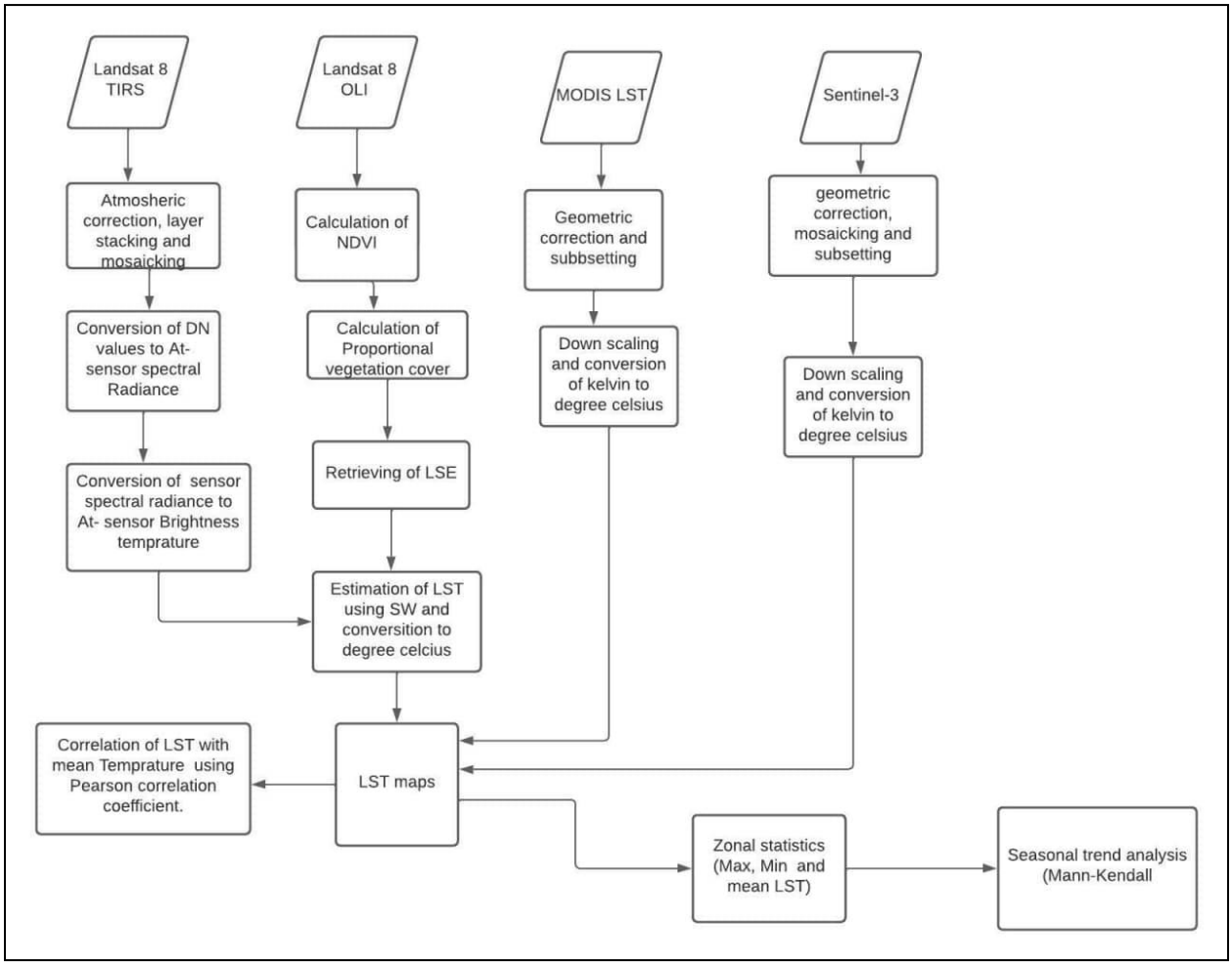

Figure 3. 5**.** Flow chart of the proposed method for estimating the LST of the study area.

CHAPTER FOUR

4 Results

4.1 NDVI of the study area.

The NDVI values of the pixel vary between −1 and +1. Figures 4.1 and 4.2 show the NDVI value of Landsat 8 OLI in two seasons of the study area. The maximum NDVI was observed in March with 0.6 (Fig 4.1c), during the dry season, whereas August in wet (rainy) with a value of 0.7 (Fig 4.2c). In 2021 the NDVI range between −0.34 to +0.59 in January, −0.2 to +0.51 in February, −0.43 to +0.6 in March, and −0.61 to +0.56 in April of the dry season. The maximum NDVI value decreased from 0.59 in January to 0.51 in February. While the minimum NDVI value increased from -0.34 to -0.20 between January and February. But the maximum NDVI value increased from 0.51 to 0.60 between February and March. Whereas the minimum NDVI decreased from -0.2 to -0.43 between February and March. Both the maximum and minimum NDVI values were decreased with the maximum from 0.60 to 0.56 and the minimum from -0.43 to -0.61 between March and April. But in general, the mean NDVI values were decreased from 0.13 to 0.09 between January to February and the same or equal with the value 0.09 from February to April (Table 4.1). Therefore, it can be said that the NDVI is decreasing and equal in the Tana sub-basin over the dry season months.

The NDVI value in wet (rainy) lies between -0.30 to 0.60 in June, -0.54 to 0.53 in July and -0.12 to 0.70 in August (Fig 4.2). The maximum NDVI value decreased from 0.60 to 0.53 between June and July. similarly, the minimum NDVI value decreased from -0.30 to -0.54 from June to July. The maximum NDVI value increased from 0.53 to 0.70 from July to August, similarly, the minimum value was increased from -0.54 to -0.12. The mean NDVI values decreased from 0.12 to 0.10 between June and July, whereas, increased from 0.10 to 0.33 between July and August. Finally, it can be concluded that the NDVI value is increased from the dry season to the wet (rainy) or . All those NDVI was used for LSE estimation.

Table 4.1 NDVI values of the dry and wet (rainy) seasons

	Min	Max	Mean
January	-0.34	0.59	0.13
February	-0.20	0.51	0.09
March	-0.43	0.60	0.09
April	-0.61	0.56	0.09
June	-0.30	0.60	0.12
July	-0.54	0.53	0.10
August	-0.12	0.70	0.33

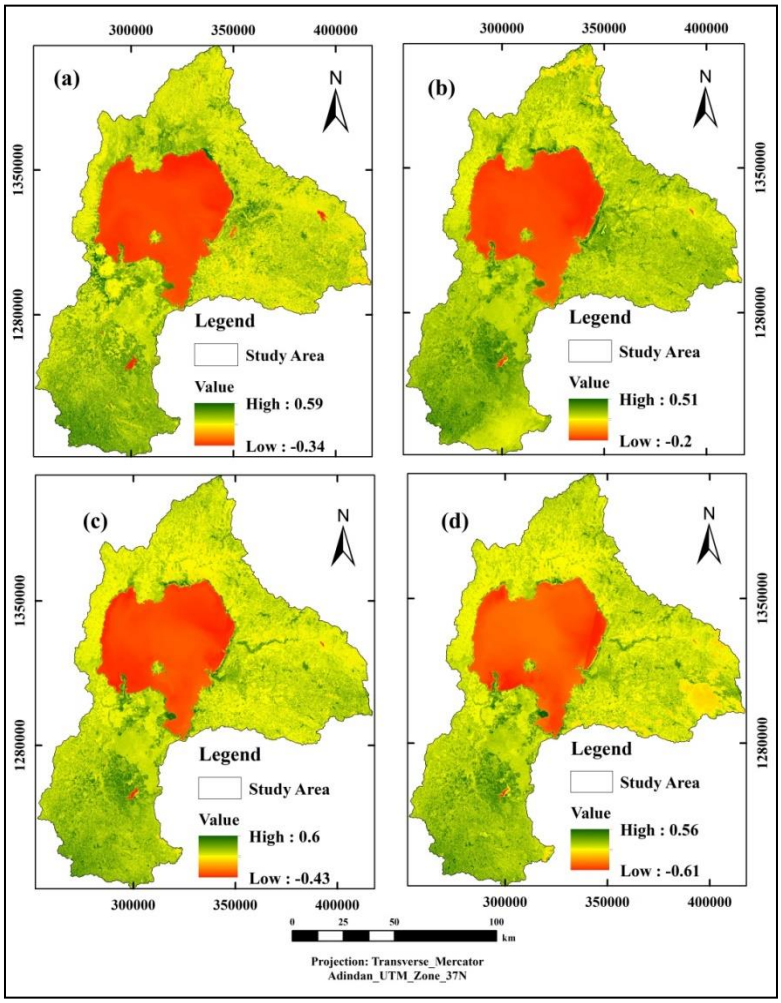

Figure 4.1 NDVI of the dry season (a) January, (b) February, (c) March, and (d) April.

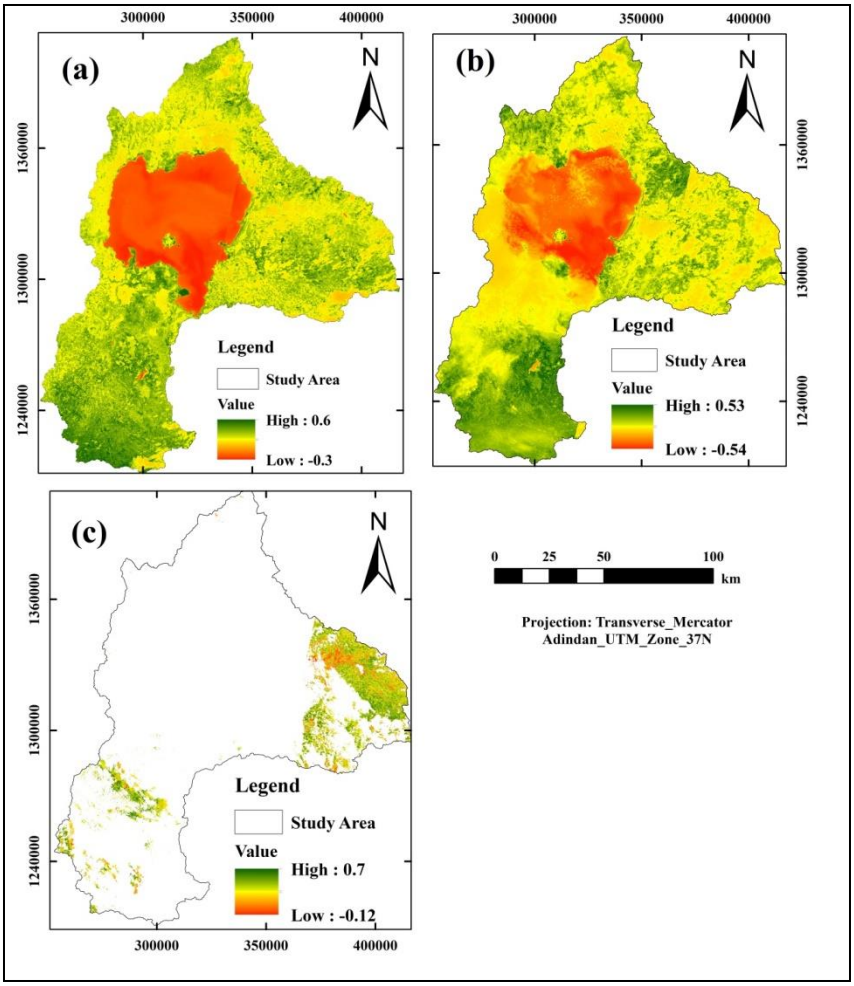

Figure 4.2 NDVI of the wet (rainy) season (a) June, (b) July, and (c) August.

4.2 Land surface emissivity

Figure 4.3 shows land surface emissivity of January, February, March, and April of the dry season generated from band 10. On the other hand, Figure 4.4 shows land surface emissivity of January, February, March, and April of the dry season generated from band 11. Figure 4.5 and Figure 4.6 show the LSE of band 10 and band 11 in June, July, and August of the wet (rainy) season. Appendix 3 shows the mean LSE value between 0.979 to 0.999 in January, 0.982 to 0.989 in February, 0.984 to 0.989 in March, and 0.983 to 0.990 in April of the dry season. Appendix 4 shows the mean LSE of wet (rainy) which lies from 0.984 to 0.997 in June, 0.974 to 0.987 in July and 0.974 to 0.997 in August. The minimum land surface emissivity is observed in the central parts (Lake Tana) of the study area. Mean LSE and difference LSE were used for LST estimation.

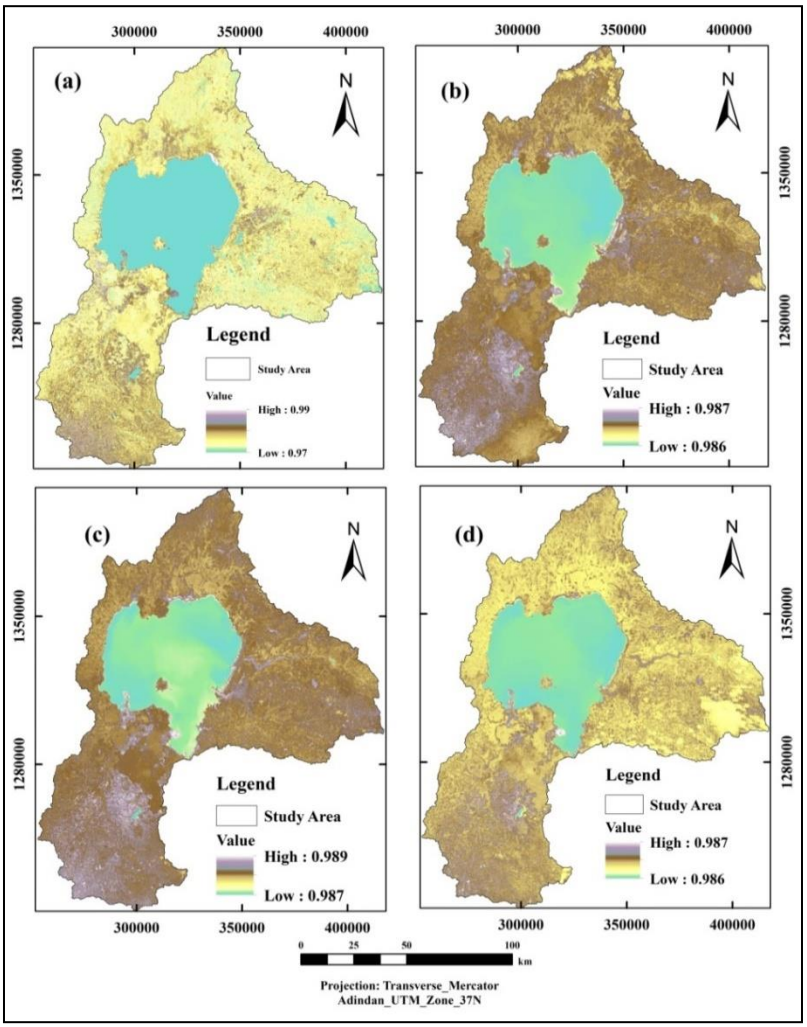

Figure 4.3 LSE of band 10 in the dry season (a) January,(b) February, (c) March and (d) April

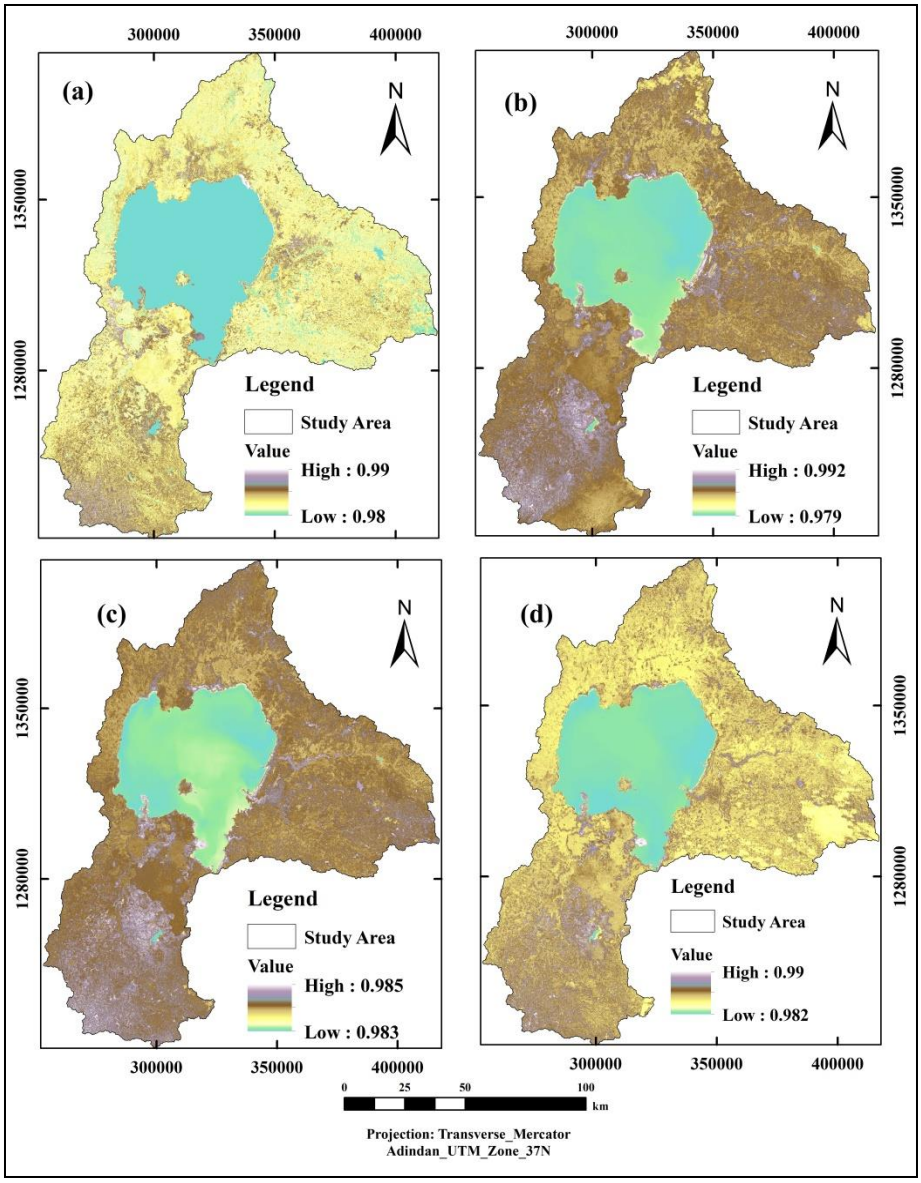

Figure 4.4 LSE of band 11 in the dry season (a) January,(b) February, (c) March and (d) April

.

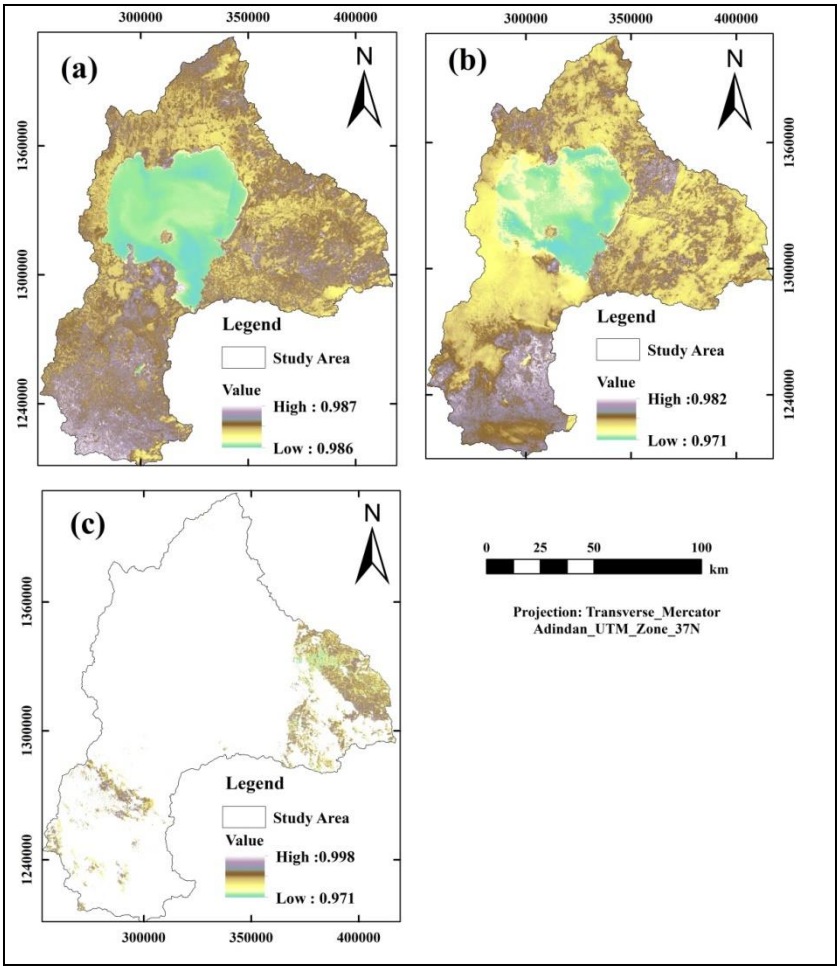

Figure 4.5 LSE of band 10 in wet (rainy) (a) June,(b) July and (c) August.

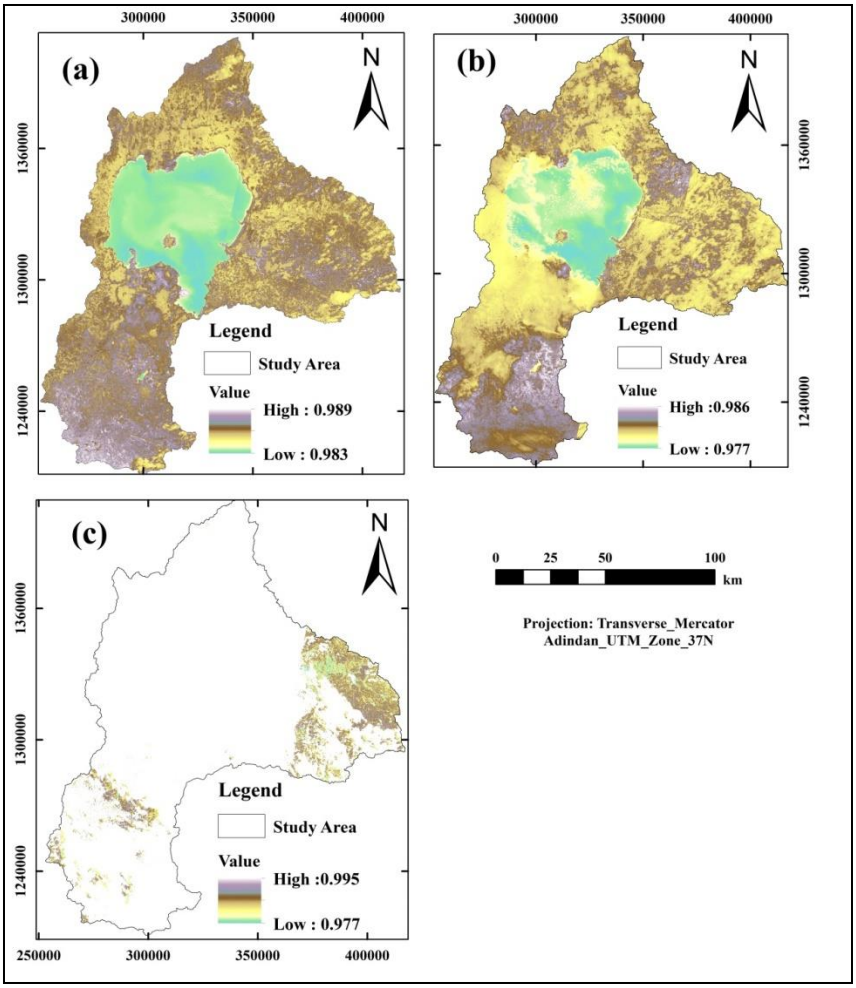

Figure 4.6 LSE of band 11 in wet (rainy) (a) June,(b) July and (c) August.

4.3 At-top of satellite brightness temperature

The At-top of satellite brightness temperature during dry season derived from bands 10 and 11 are shown in Fig 4.7 and Fig 4.8 for January, February, March and April. The At-top of satellite brightness temperature of the wet (rainy) season is shown in Fig 4.9 and Fig 4.10 for the three months.

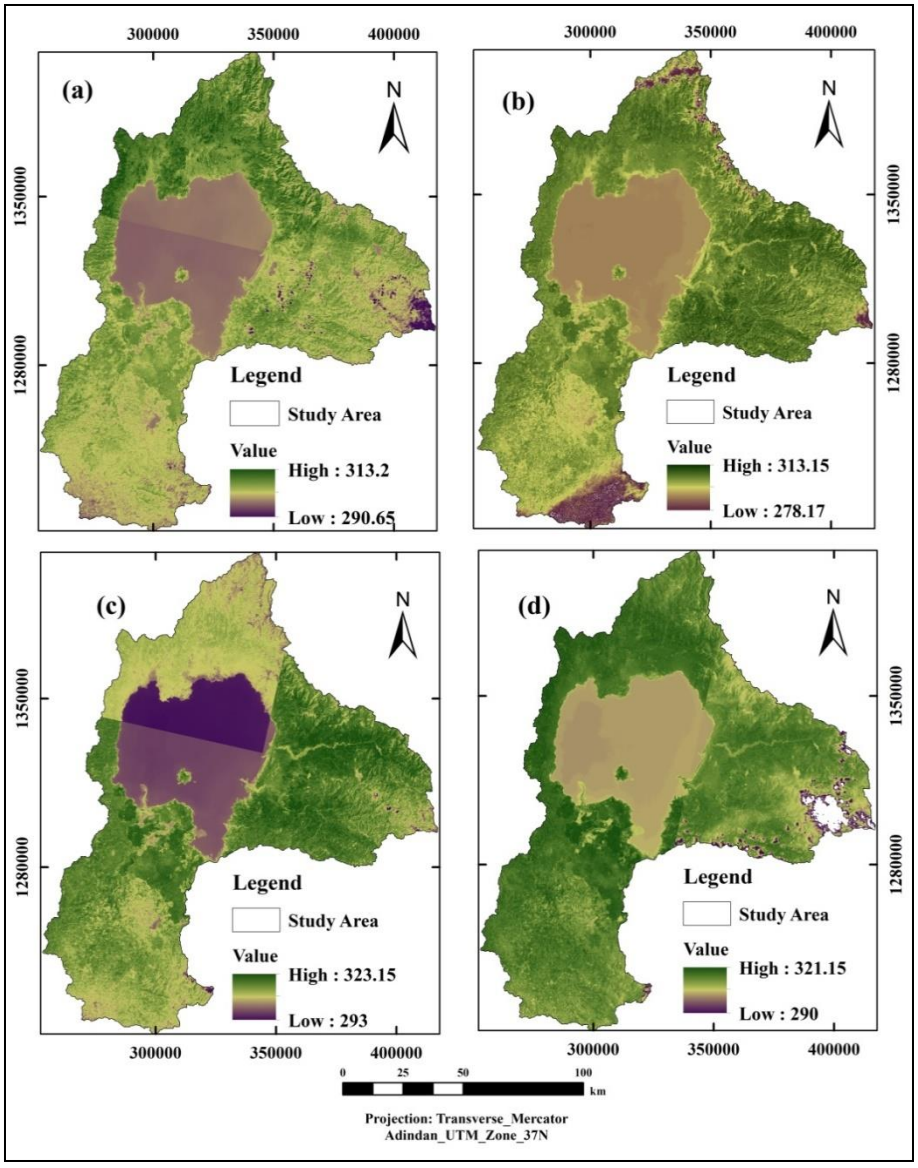

Figure 4. 7 At top of atmosphere brightness temperature in the dry season of band 10 (a) January, (b) February, (c) March and (d) April.

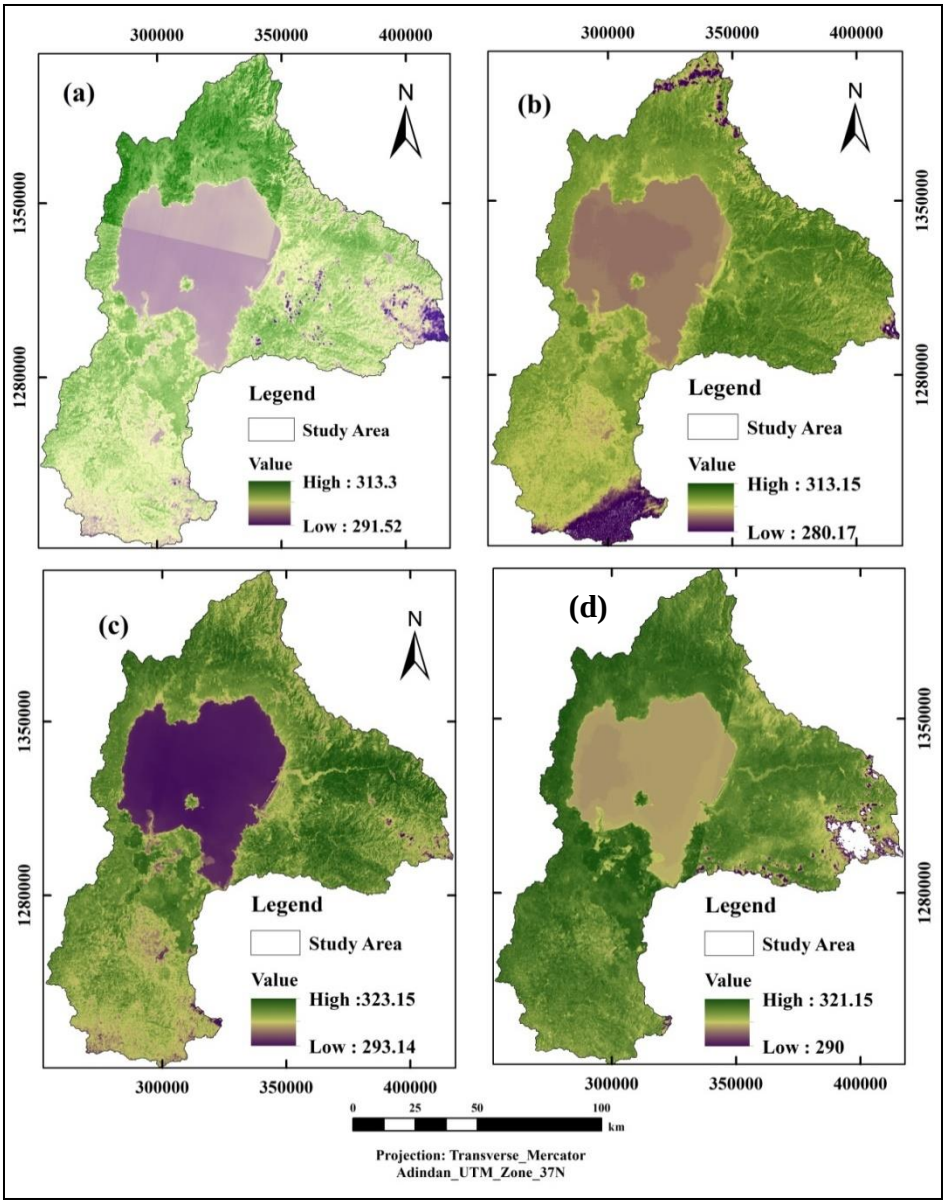

Figure 4.8At top of atmosphere brightness temperature in the dry season of band 11 (a) January, (b) February, (c) March, and (d) April.

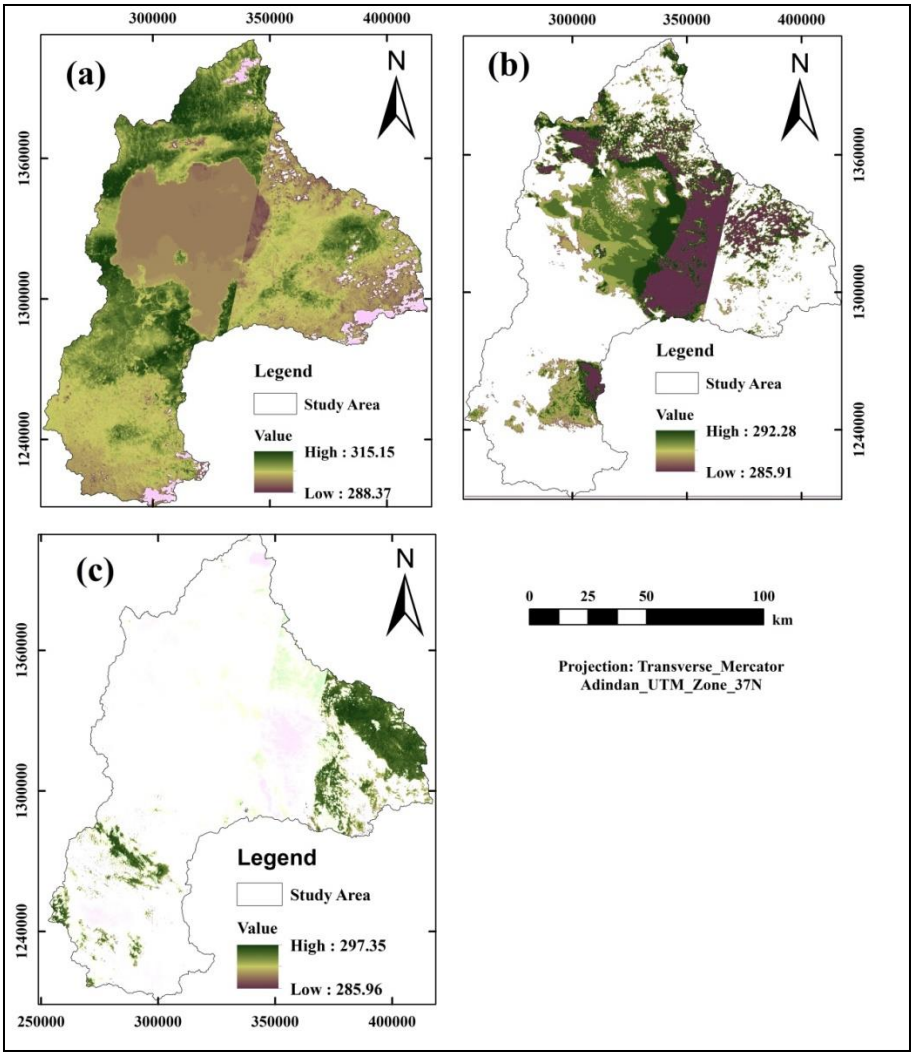

Figure 4.9 At top of atmosphere brightness temperature in wet (rainy) of band 10 (a) June, (b) July, and (c) August.

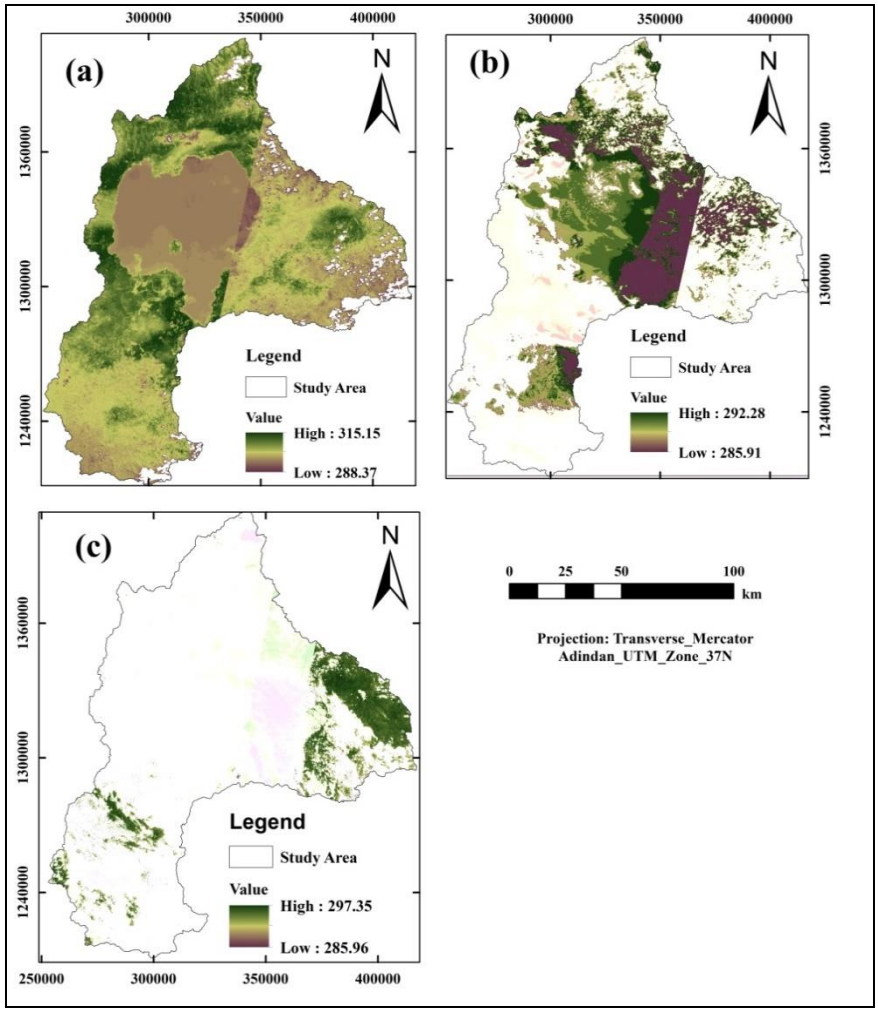

Figure 4.10 At top of atmosphere brightness temperature in wet (rainy) season of band 11 (a) June, (b) July, and (c) August.

4.4 Land surface temperature (LST)

Table 4.2 shows the spatial and seasonal LST values of the study area. The LST distributions of the four months' results are shown in Figs 11, 12, 13 and 14 for the Landsat 8 TIRs, MODIS and Sentinel-3. Whereas Figs 14.15,16 and 17 presents the wet (rainy) season LST. The maximum LST of the dry season was observed in Sentinel-3 of April with 51°C and the lowest LST was observed in Landsat 8 TIRs of February with 5°C. Whereas the maximum temperature in wet (rainy) was seen in Landsat 8 of June at 42°C and the minimum was in Sentinel-3 of July with 8°C.

The mean maximum LST during the dry season was recorded in MODIS of March with the value 37.32°C followed by Sentinel-3 of March with 37.30°C. Whereas in the case of wet (rainy), the mean maximum was observed in June of MODIS with 27.51°C followed by June of Landsat 8 with 25.73°C.

The study result reveals that the LST for the dry season for Landsat 8 TIRs, ranging from 17.05 to 40.50°C in January (fig 4.11 a), 5 to 40 °C in February (fig 4.12 a), 19 to 50°C in March (fig 4.13 a) and 16 to 48°C in April (fig 4.14 a). The mean LST for Landsat 8 was shown in Table 4.2 with the values 25.14°C in January, 27°C in February, 35.31°C in March and 35.47°C in April of the dry season. Likewise, for MODIS its LST results vary from 19.93 to 41°C in January (fig 4.11b), 18.17 to 44.60°C in February (fig 4.12b), 21.09 to 48.40°C in March (fig 4.13b) and 20.12 to 48.21°C in April (fig 4.14b). The mean MODIS LST was 30.77°C in January, 33.12°C in February, 37.32°C in March and 35.40°C in April (Table 4.2). Similarly, for Sentinel-3 the LST varies from 20.33 to 44.09°C in January (fig 4.11c), 16.0 to 46.80°C in February (fig 4.12 c), 16.80 to 48.41°C in March (fig 4.13 c) and 11.00 to 51.00°C in April (fig 4.14 c).

Whereas in wet (rainy) for Landsat 8 TIRs, it varies from 15.50 to 42.00°C in June (fig 4.15 a), 13.00 to 27.00°C in July (fig 4.16 a) and 12.80 to 24.20°C in August (fig 4.17 a) and the mean LST were 25.73°C in June, 15.10°C in July and 18.74 in August (Table 4.2). Correspondingly for MODIS, it varies from17.75 to 37.42°C in June (fig 4.15 b), 11.71 to 22.80°C in July (fig 4.16 b) and 13.90 to 26.78 °C in August (fig 4.17 b). The mean LST was 27.51°C in June, 17.83°C in July and 20.25°C in August (Table 4.2). For Sentinel-3, the LST results vary from 8.00 to 25.00°C in July (fig 4.16 c) and 11.30 to 22.10°C in August (fig 4.17 c) and the mean were 10.03°C in July and17.24°C in August (Table4.2).

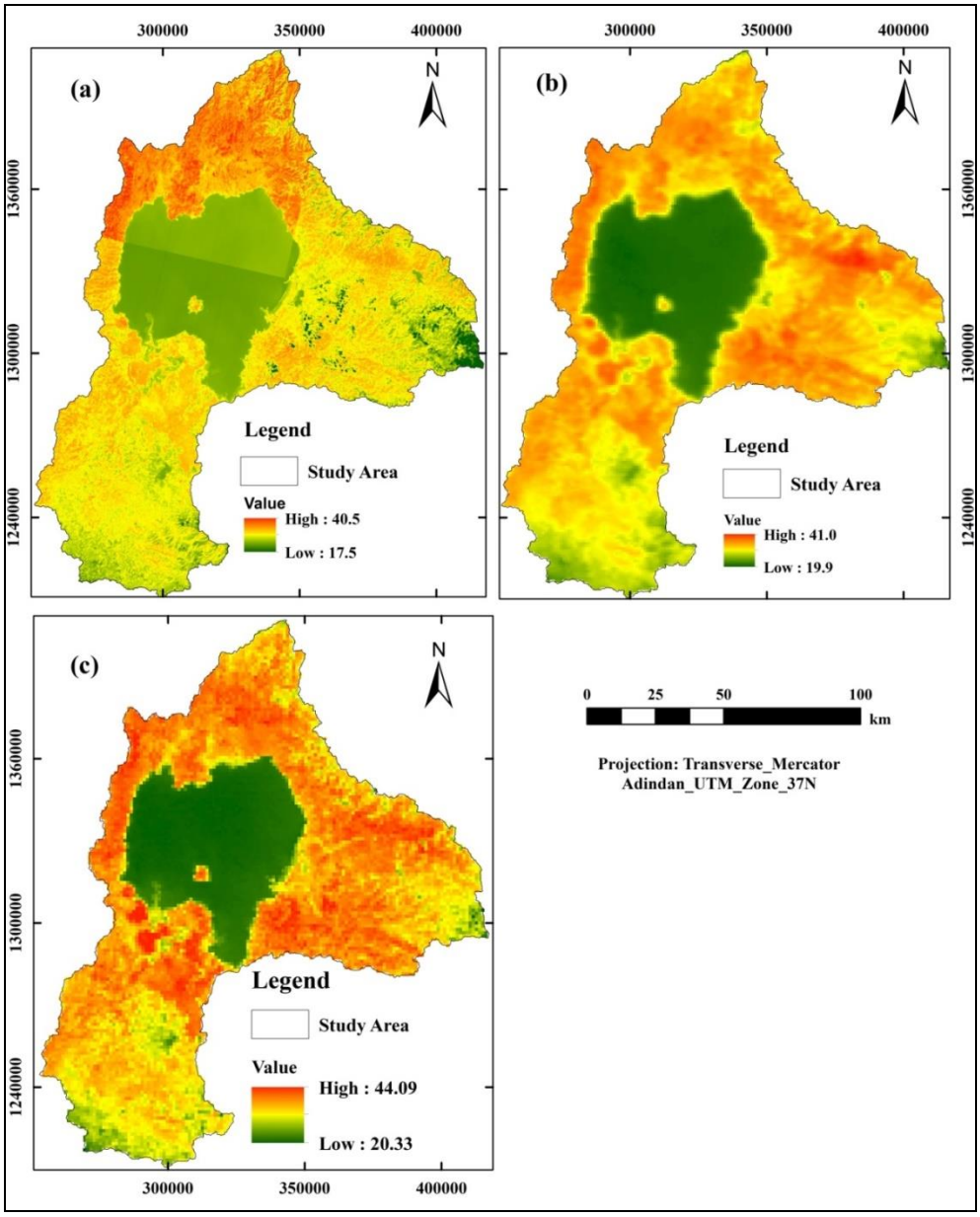

Figure 4.11 LST of January derived from Landsat 8 TIRs (a), MODIS (b), and sentinel-3 (c).

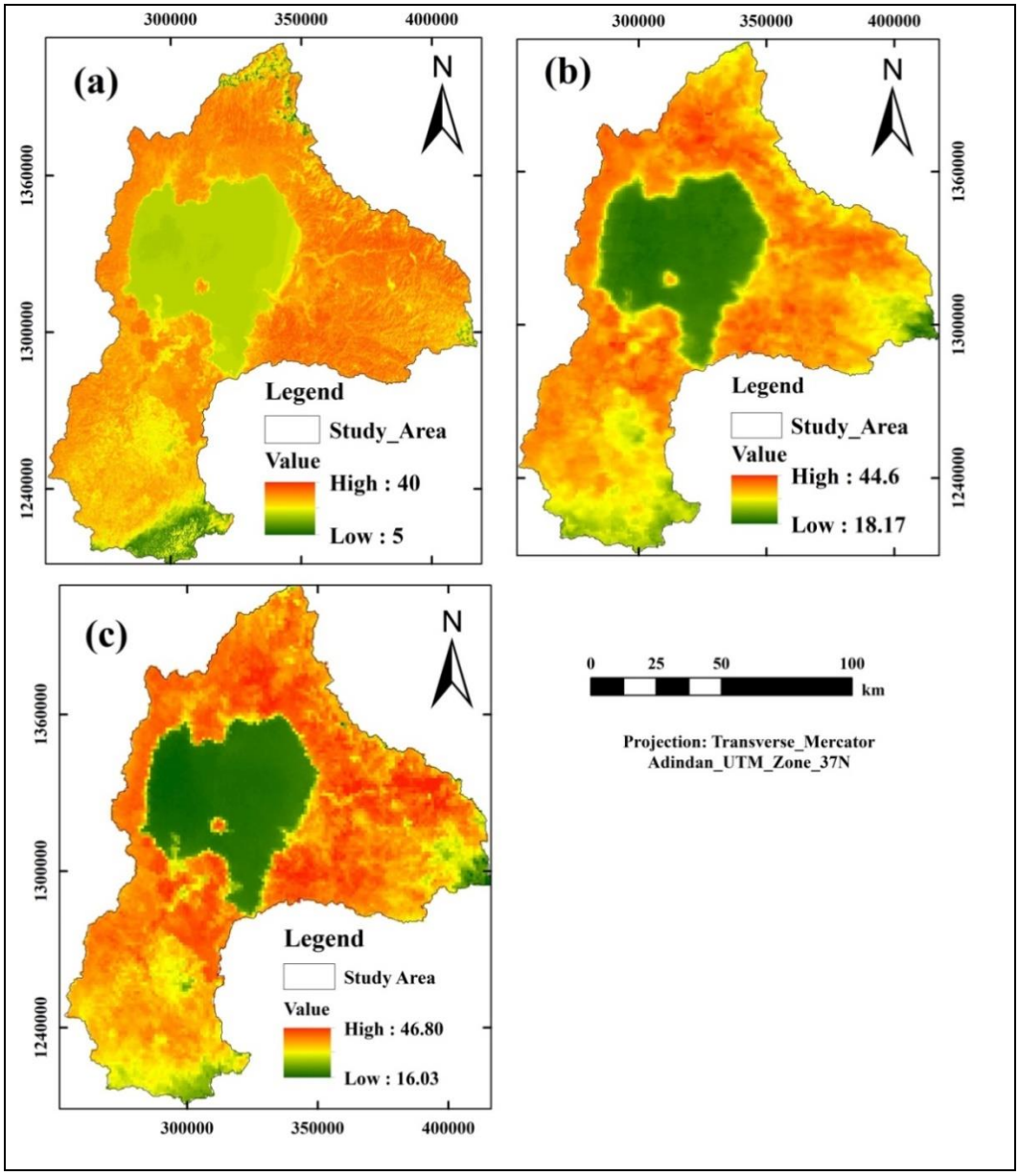

Figure 4.12 LST of February derived from Landsat 8 TIRs (a), MODIS (b) and Sentinel-3 (c).

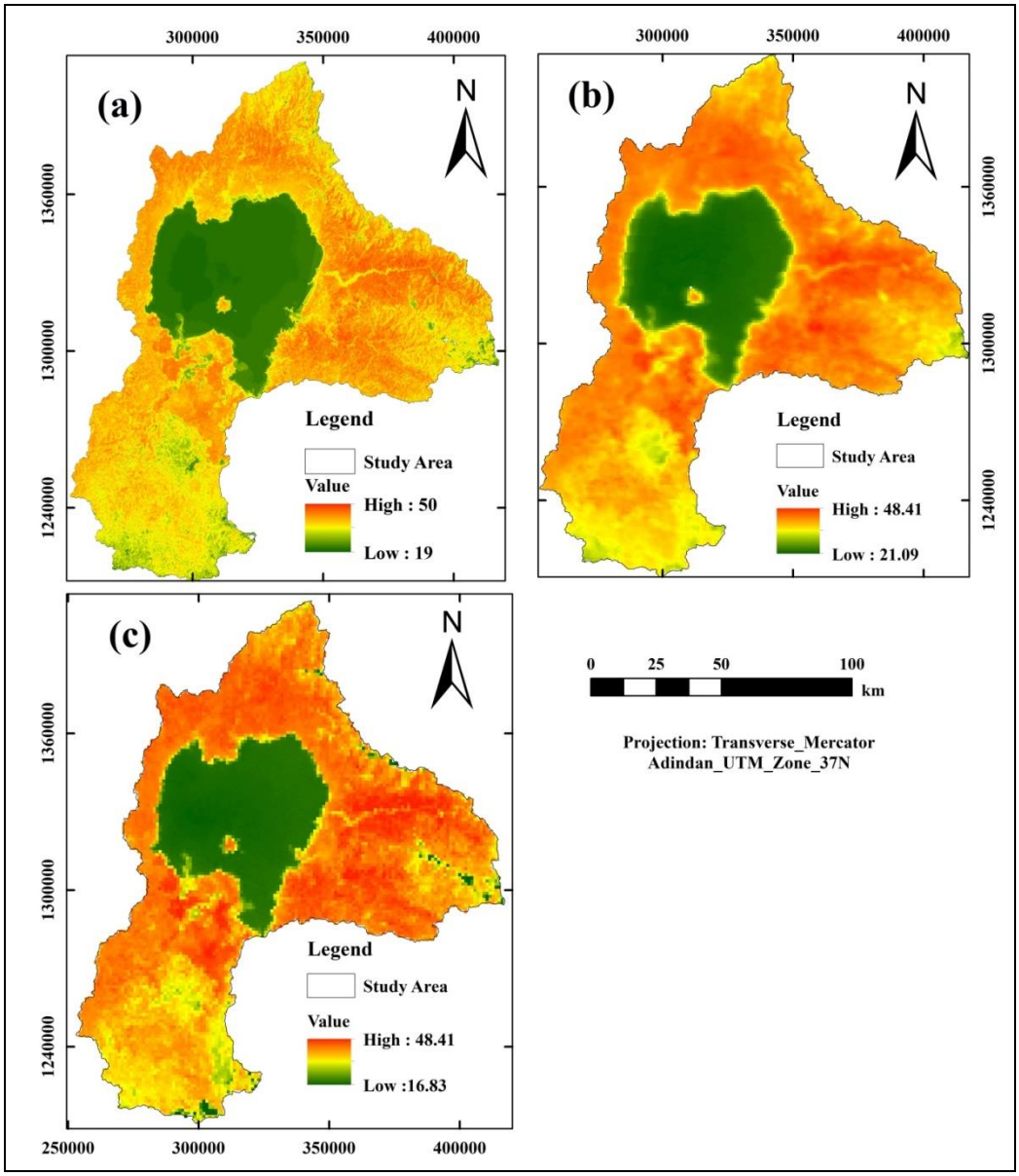

Figure 4.13 LST of March derived from Landsat 8 TIRs (a), MODIS (b) and Sentinel-3 (c).

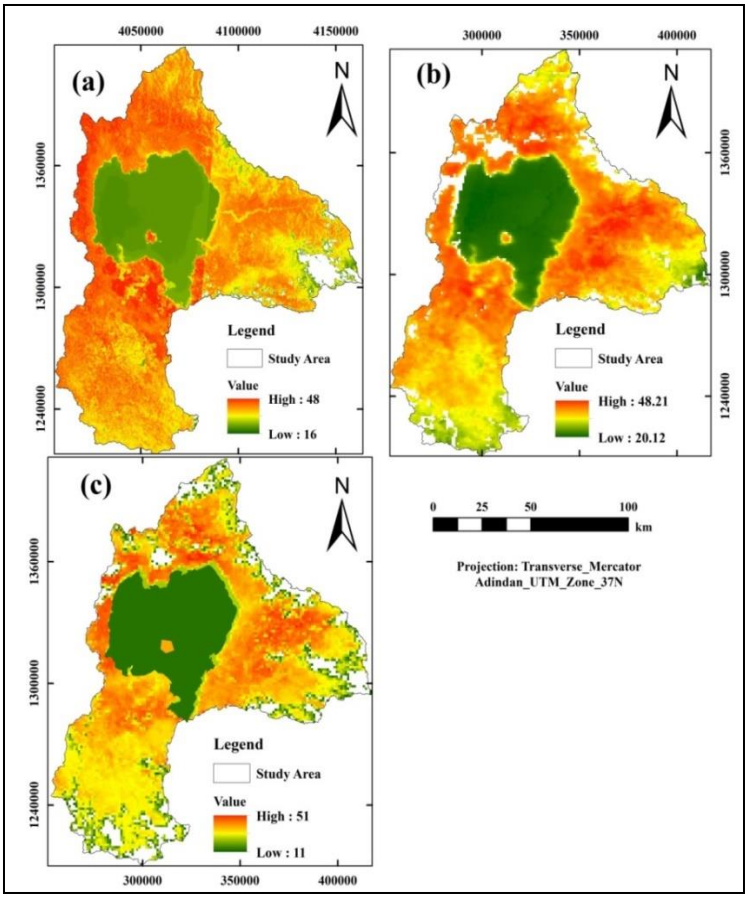

Figure 4.14 LST of April derived from Landsat 8 TIRs (a), MODIS (b) and Sentinel-3 (c).

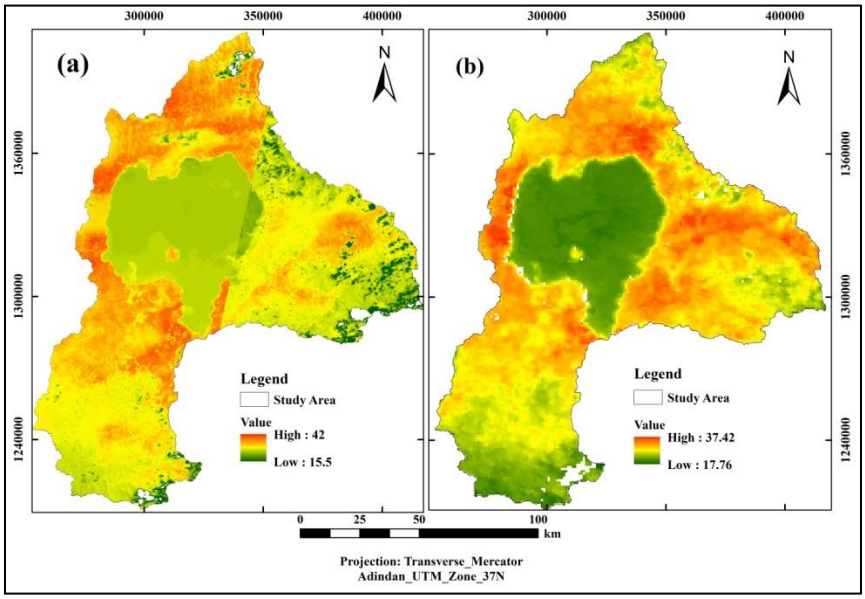

Figure 4.15 LST of June derived from Landsat 8 TIRs I (a), MODIS (b) and Sentinel-3 (c).

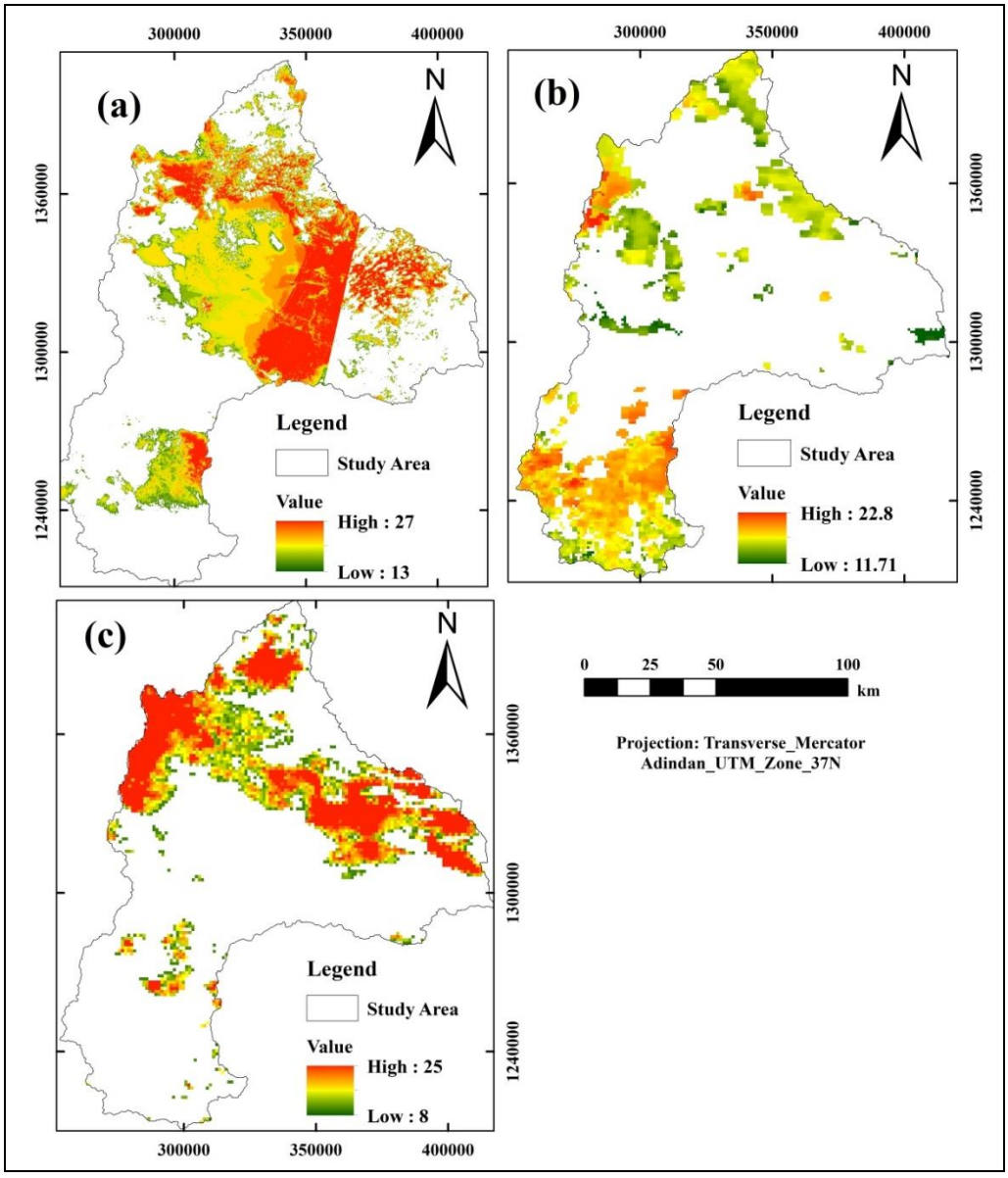

Figure 4.16 LST of July derived from Landsat 8 TIRs (a), MODIS (b) and Sentinel-3 (c).

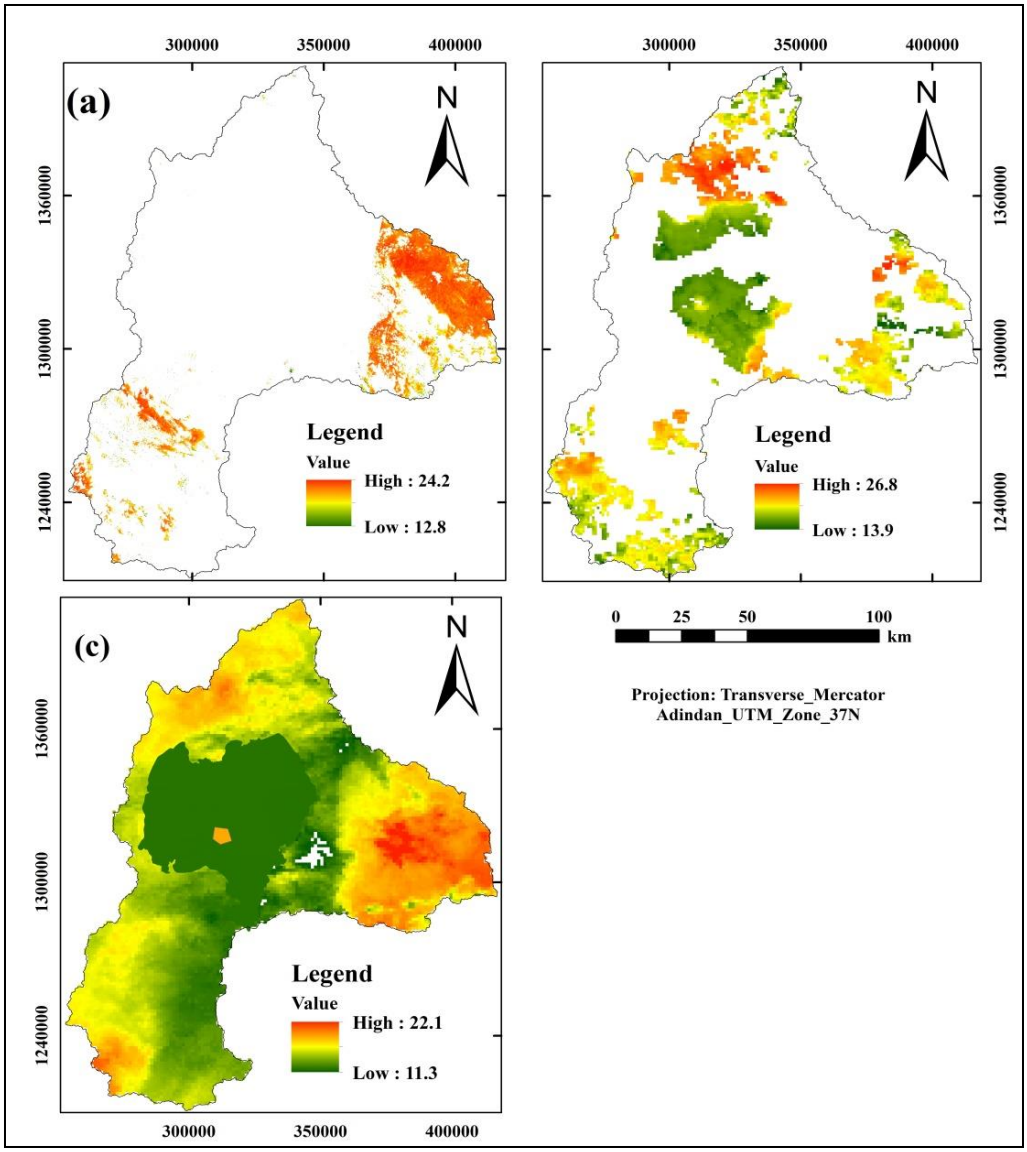

Figure 4.17 LST of August derived from Landsat 8 TIRs (a), MODIS (b) and Sentinel-3 (c).

Table 4. 2 Spatial and inter-seasonal LST (°C) values of the study area.

Sensors	Min	Max	Mean	Months
Landsat	17.05	40.50	25.14	January
MODIS	19.93	41.00	30.77	
Sentinel	20.33	44.09	33.37	
Landsat	5.00	40.00	27.00	February
MODIS	18.17	44.60	33.12	
Sentinel	16.03	46.80	35.39	
Landsat	19.00	50.00	35.31	March
MODIS	21.09	48.40	37.32	
Sentinel	16.80	48.41	37.30	
Landsat	16.00	48.00	35.47	April
MODIS	20.12	48.21	35.40	
Sentinel	11.00	51.00	30.69	
Landsat	15.50	42.00	25.73	June
MODIS	17.75	37.42	27.51	
Landsat	13.00	27.00	15.10	
MODIS	11.71	22.80	17.83	July
Sentinel	8.00	25.00	10.03	
Landsat	12.80	24.20	18.47	August
MODIS	13.90	26.78	20.25	
Sentinel	11.30	22.10	17.24	

4.5 Spatial and inter-seasonal variability's of LST.

The highest mean LST from Landsat 8 was observed in Woyna-Dega (Subtropical) Agro climatic zone in April with 36.04°C. Whereas the lowest mean LST was seen in Kur Agro climatic zone during June with the LST 8.55°C. For MODIS the highest mean LST was observed in Woyna-Dega (Subtropical) Agro climatic zone during April with 35.76°C. On the other hand, the lowest mean LST was observed in Dega (Cool) Agro climatic zone during July with16.42°C. For Sentinel-3 the highest mean LST was seen in Woyna-Dega (Subtropical) Agro climatic zone during March with LST 37.83. Whereas, the lowest were in Wurch and Kur Agro climatic zone with LST 8°C (Table 4.3).

Table 4. 3 Mean LST (°C) across different Agro climatic zone.

Months	ACZ	Landsat 8 LST	MODIS LST	Sentinel-3 LST
January	Woyna-Dega	25.39	30.79	33.42
	Dega	24.21	30.78	33.19
	Wurch	25.02	25.06	28.78
	Kur	17.00	22.06	25.87
February	Woyna-Dega	27.49	33.43	35.48
	Dega	24.72	31.66	35.10
	Wurch	16.51	21.76	24.26
	Kur	10.18	21.61	21.43
March	Woyna-Dega	35.94	37.93	37.83
	Dega	35.21	37.21	37.19
	Wurch	30.72	32.58	32.68
	Kur	27.21	30.74	27.97
April	Woyna-Dega	36.04	35.76	32.65
	Dega	32.81	33.26	20.27
	Wurch	19.84	24.84	11.62
	Kur	16.48	27.48	11.33
June	Woyna-Dega	26.62	27.78	
	Dega	21.46	26.12	
	Wurch	10.03	24.06	
	Kur	8.55	21.76	
July	Woyna-Dega	15.42	17.9	10.21
	Dega	13.44	16.42	9.11
	Wurch	13	null	8
	Kur	13	null	8
August	Woyna-Dega	23.48	20.41	19.35
	Dega	22.65	19.46	15
	Wurch	21.48	null	13
	Kur	18.35	null	12.18

Remark: the null results are due to cloud effect.

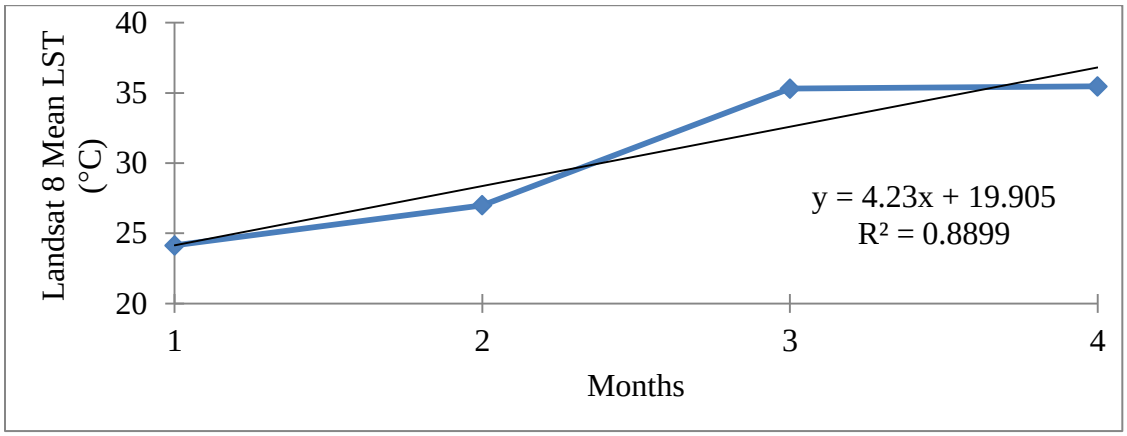

Figure 4.18 Mann Kendall mean monthly Landsat 8 LST trends during January (1), February (2), March (3) and April (4) of the dry season.

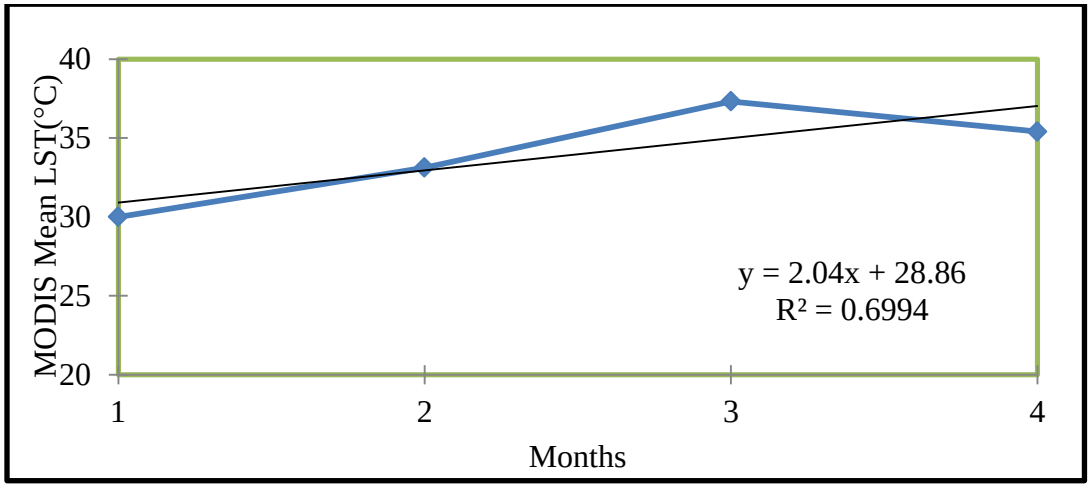

Figure 4.19 Mann Kendall mean monthly MODIS LST trends during January (1), February (2), March (3) and April (4) of the dry season

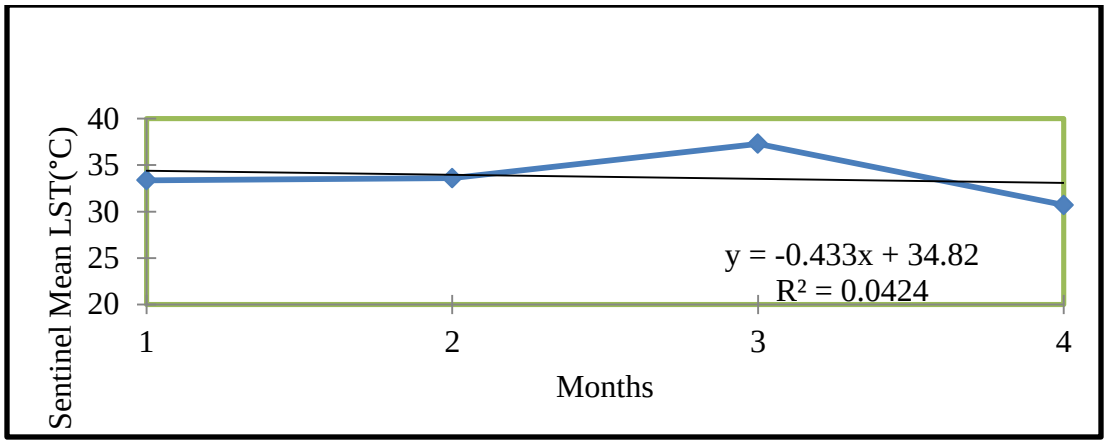

Figure 4.20 Mann Kendall mean monthly Sentinel-3 LST trends during January (1), February (2), March (3) and April (4) of the dry season

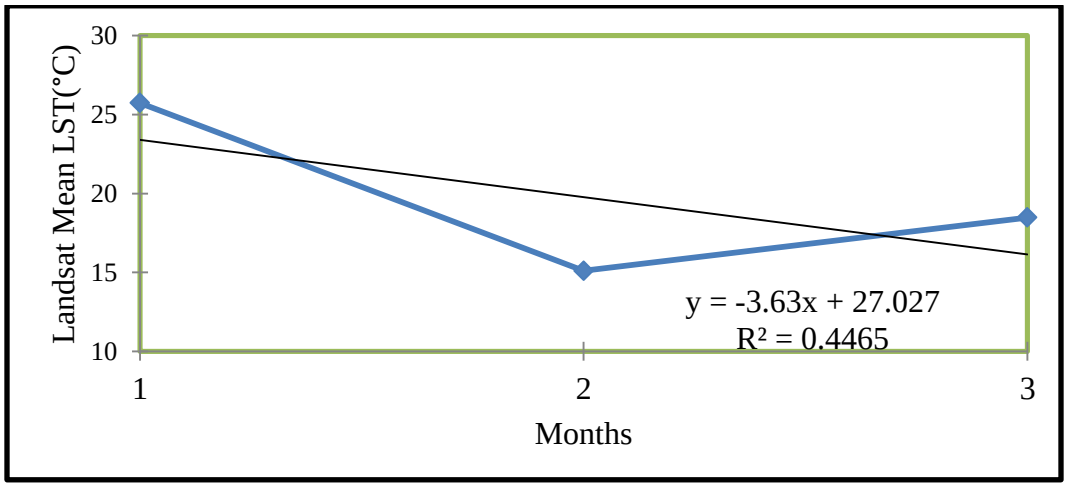

Figure 4.21 Mann Kendall mean monthly Landsat 8 LST trends during June (1), July (2), and August (3) of the wet (rainy) season

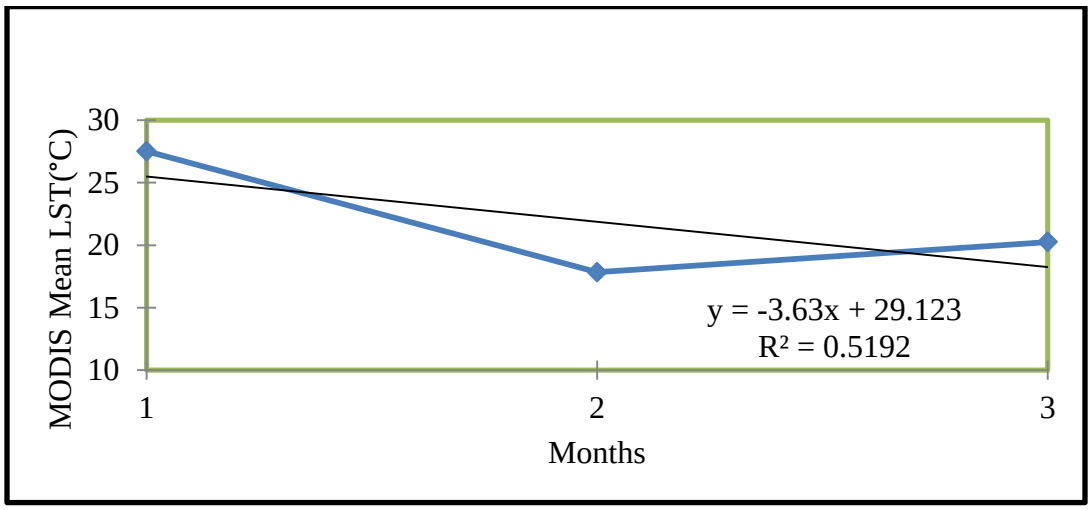

Figure 4.22 Mann Kendall mean monthly MODIS LST trends during June (1), July (2) and August (3) of the wet (rainy) season

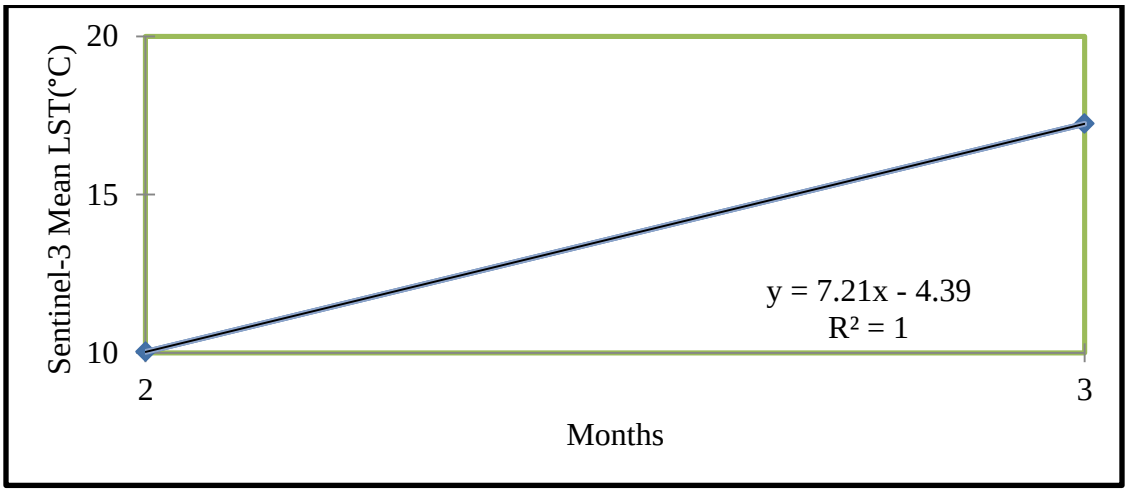

Figure 4.23 Mann Kendall mean monthly Sentinel-3 LST trends during July (2) and August (3) of the wet (rainy) season

Table 4. 4 Mann Kendall Min LST trend test for the dry season at significant level α =0.05

Variables	Landsat 8 LST	MODIS LST	Sentinel-3 LST
Kendall's tua	0	0.333	-0.667
S	0.000	2.000	-4.000
P-value	1.000	0.734	0.308
Min	5.000	18.170	11.000
Max	19.000	21.090	20.330
Mean	14.263	19.828	16.040
Sen's slope (change/month)	0.3125	0.322	-2.813

Table 4. 5 Mann Kendall Min LST trend test for the wet (rainy) season at significant level α =0.05.

Variables	Landsat 8 LST	MODIS LST	Sentinel-3 LST
Kendall's tua	-1	-0.333	1
S	-3.000	-1.000	1.000
P-value	0.296	1.000	1.000
Min	12.800	11.710	8.000
Max	15.500	17.750	11.300
Mean	13.767	14.453	9.650
Sen's slope (change/month)	-1.35	-1.925	3.300

The result indicates a p-value greater than the significance level α = 0.05 then null hypothesis H0 cannot be rejected and the reverse is true for H1. The minimum LST of Landsat 8 revealed a statistically no trend with a P-value of 1 which is greater than 0.05 with S is 0. Whereas, MODIS LST MK trend test shows that statistically insignificant increasing trend with a P-value of 0.734 which is greater than 0.05 with S is 2. But Sentinel-3 LST shows statistically insignificant decreasing trend with a P-value of 0.308 which is greater than 0.05 with S is -4 and H_0 is accepted in the dry season (Table 4.4).

Whereas, in wet (rainy) season the minimum LST of Landsat 8 revealed a statistically insignificant decreasing trend with a P-value of 0.296 which is greater than α= 0.05 with S is -3. Similarly, for MODIS indicates statistically insignificant decreasing trend with a P-value of 1 with S value -1. But Sentinel-3 minimum LST shows statistically insignificant increasing trend with a P-value of 1 with S value 1 in wet (rainy) season (Table 4.5).

Table 4. 6 Mann Kendall Max LST trend test for the dry season at significant level α =0.05.

Variables	Landsat 8 LST	MODIS LST	Sentinel-3 LST
Kendall's tua	0.333	0.667	1
S	2.000	4.000	6.000
P-value	0.734	0.308	0.089
Min	40.000	41.000	44.090
Max	50.000	48.400	51.000
Mean	44.625	45.553	47.575
Sen's slope (change/month)	3.25	3.001666667	2.232

Table 4. 7 Mann Kendall Max LST trend test for the wet (rainy) season at significant level α =0.05.

Variables	Landsat 8 LST	MODIS LST	Sentinel-3 LST
Kendall's tua	-1	-0.333	-1
S	-3.000	-1.000	-1.000
P-value	0.296	1.000	1.000
Min	24.200	22.800	22.100
Max	42.000	37.420	25.000
Mean	31.067	29.000	23.550
Sen's slope (change/month)	-8.9	-5.32	-2.900

When the result indicates a p-value greater than the significance level $\alpha = 0.05$ then null hypothesis H0 cannot be rejected and vice versa for H1. The maximum LST of Landsat 8 revealed a statistically insignificant increasing trend with a P-value of 0.734 which is greater than 0.05 and with S value 2. Likewise, MODIS LST MK trend test shows that statistically insignificant increasing trend with a P-value of 0.308 which is greater than 0.05 with S is 4. Similarly, Sentinel-3 LST shows statistically insignificant increasing trend with a P-value of 0.089 which is greater than 0.05 and with S value 6 and H_0 is accepted in the dry season (Table 4.6). Whereas, in wet (rainy) the maximum LST of Landsat 8 revealed a statistically insignificant decreasing trend with a P-value of 0.296 which is greater than $\alpha = 0.05$ with S is -3. Similarly, for MODIS indicates statistically insignificant decreasing trend with a P-value of 1 with S value -1. Likewise, Sentinel-3 maximum LST shows statistically insignificant decreasing trend with a P-value of 1 with S = -1 in wet (rainy) season (Table 4.7).

Table 4. 8 Mann Kendall Mean LST trend test for the dry season at significant level $\alpha = 0.05$.

Variables	Landsat 8 LST	MODIS LST	Sentinel-3 LST
Kendall's tua	1	0.667	0
S	6.000	4.000	0.000
P-value	0.089	0.308	1
Min	24.140	30.000	30.690
Max	35.470	37.320	37.300
Mean	30.480	33.960	33.738
Sen's slope (change/month)	4.006	2.460	-0.337

Table 4. 9 Mann Kendall Mean LST trend test for the wet (rainy) season at significant level $\alpha = 0.05$.

Variables	Landsat 8 LST	MODIS LST	Sentinel-3 LST
Kendall's tua	-0.333	-0.333	1
S	-1.000	-1.000	1.000
P-value	1.000	1.000	1.000
Min	15.100	17.830	10.030
Max	25.730	27.510	17.240
Mean	19.767	21.863	13.635
Sen's slope (change/month)	-3.63	-3.63	7.210

When the result indicates a p-value greater than the significance level $\alpha = 0.05$ then null hypothesis H0 cannot be rejected and vice versa. However, the mean LST of Landsat 8 revealed a statistically insignificant increasing trend with a P-value of 0.089 which is greater than 0.05.

Likewise, MODIS LST MK trend test shows that statistically insignificant increasing trend with a P-value of 0.308 which is greater than 0.05. But Sentinel-3 LST shows no trend and H_0 is accepted in the dry season (Table 4.8). Whereas, in wet (rainy) the mean LST of Landsat 8 revealed a statistically insignificant decreasing trend with a P-value of 1 which is greater than $\alpha = 0.05$. Similarly, for MODIS indicates statistically insignificant decreasing trend with a P-value of 1. But Sentinel-3 Mean LST shows statistically insignificant increasing trend with a P-value of 1 in wet (rainy) season (Table 4.9).

4.6 Correlations of LST with mean near surface air temperature data.

The relationship between LST of January, February, March, and April for Landsat 8, MODIS, and Sentinel-3 with mean temperature data are shown in Figs 4.24, 4.25, 4.26 and 4.27.

Table 4.10 shows the correlation between Landsat 8, MODIS and Sentinel-3 LST *vs* Mean air temperature. The maximum Pearson correlation coefficient (r) was observed in March of Landsat 8 with r = 0.73 followed by MODIS of March and Landsat 8 with r = 0.7 in the dry season. Whereas the minimum Pearson correlation coefficient (r) was observed in February of MODIS and April of Sentinel-3 with r= 51. While in wet (rainy) the maximum Pearson correlation coefficient (r) was observed in August of Landsat 8 with r= 0.66 followed by August of MODIS with r= 0.57.

The results of Pearson correlation (r) between LST and mean air temperature reveals that for Landsat 8 *vs* mean air temperature, r= 0.7 in January, 0.55 in February, 0.73 in March and 0.66 in April of the dry season. The Pearson r for MODIS *vs* mean air temperature was 0.52 in January, 0.51in February, 0.7 in March and 0.58 in April. Likewise, the r between Sentinel-3 *vs* Mean air temperature was 0.56 in January, 0.52 in February, 0.52 in March and 0.51 in April.

Although during wet (rainy) the Pearson correlation coefficient (r) for Landsat 8 *vs* mean air temperature was 0.56 in June, 0.54 in July and 0.66 in August. Similarly, the Pearson (r) for MODIS *vs* mean temperature was 0.51 in June, 0.53 in July and 0.57 in August. Likewise for Sentinel-3 *vs* mean air temperature was 0.44 in July and 0.55 in August. Therefore in general it can be concluded that the Correlation between Landsat LST 8, MODIS, and Sentinel-3 *vs* mean temperature indicated a strong positive correlation except for July of sentinel-3. The R^2 from figure 4.24 to 4.30 revealed that, there was no interdependency between LST and mean near surface air temperature.

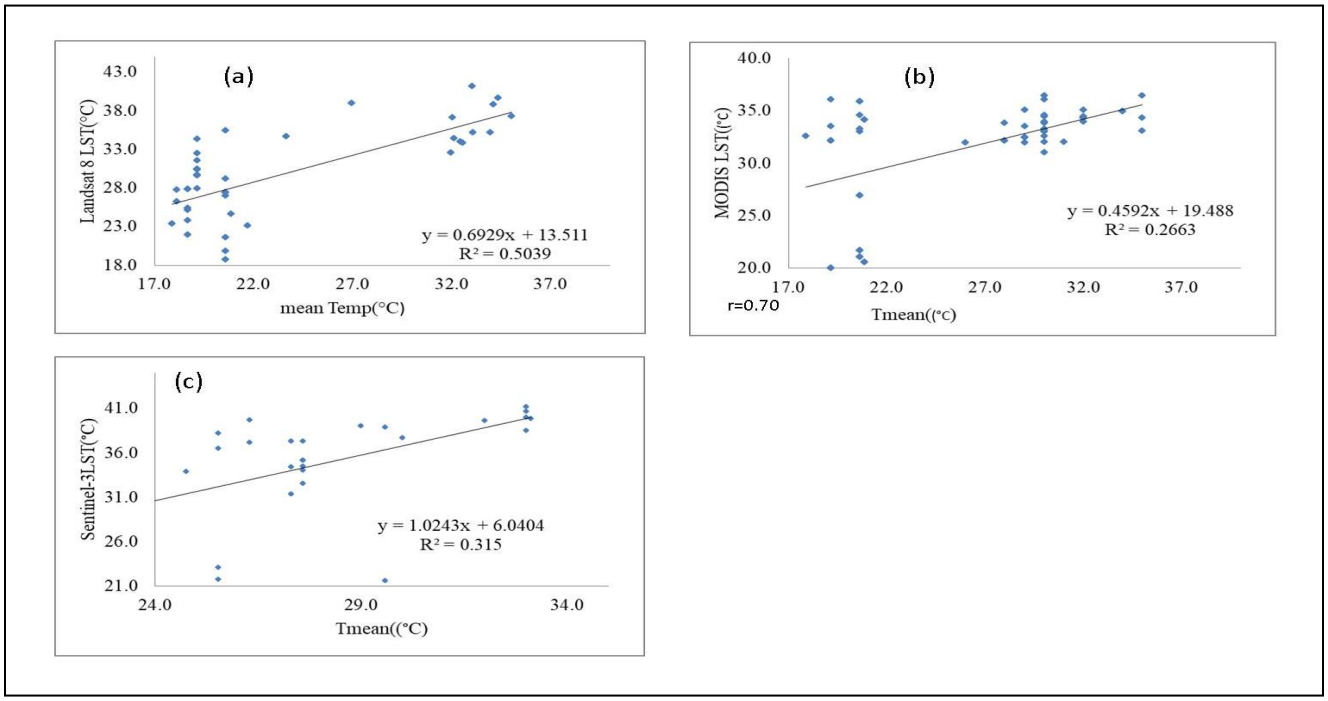

Figure 4.24 Relationship between Landsat 8 (a), MODIS (b) and Sentinel-3(c) driven LST vs. mean temperature in January.

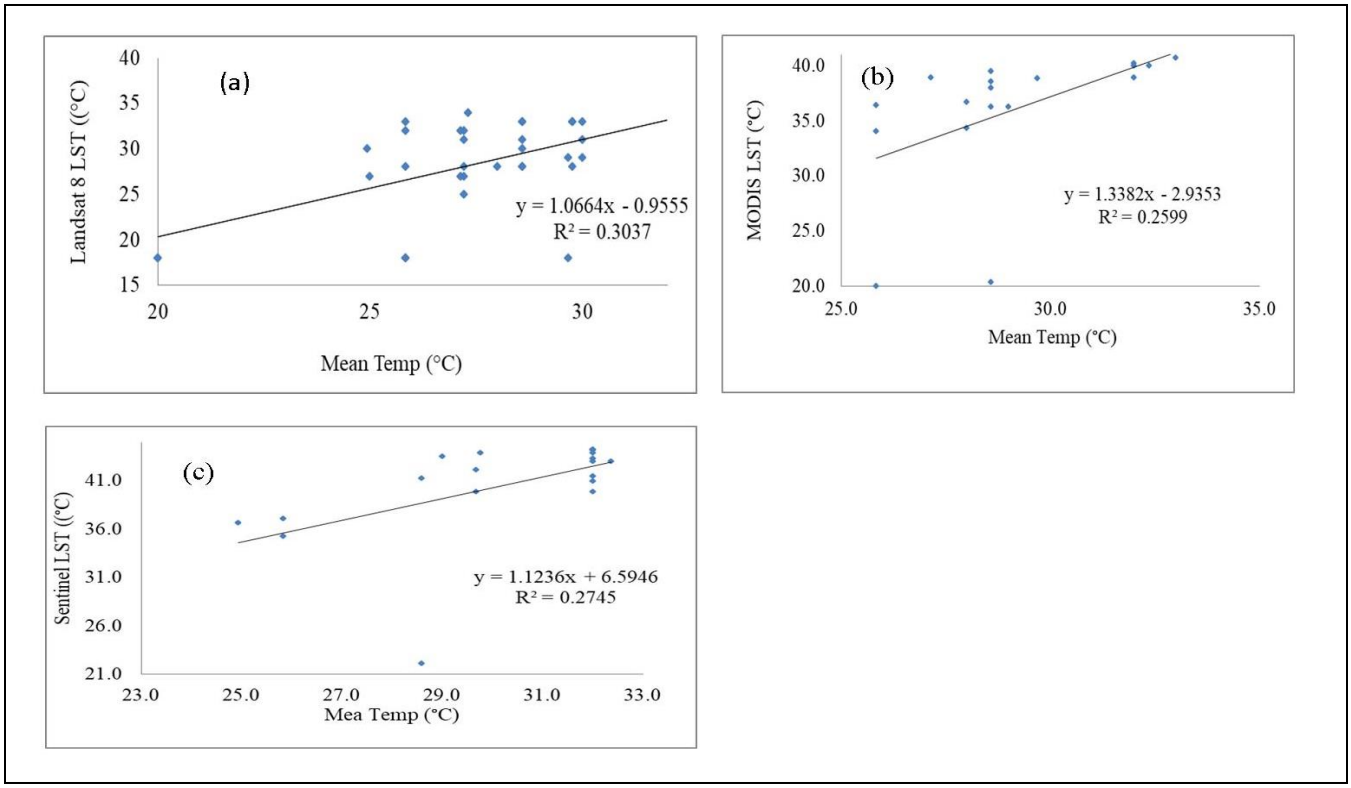

Figure 4.25 Relationship between Landsat 8 (a), MODIS (b) and Sentinel-3(c) driven LST vs. mean temperature in February.

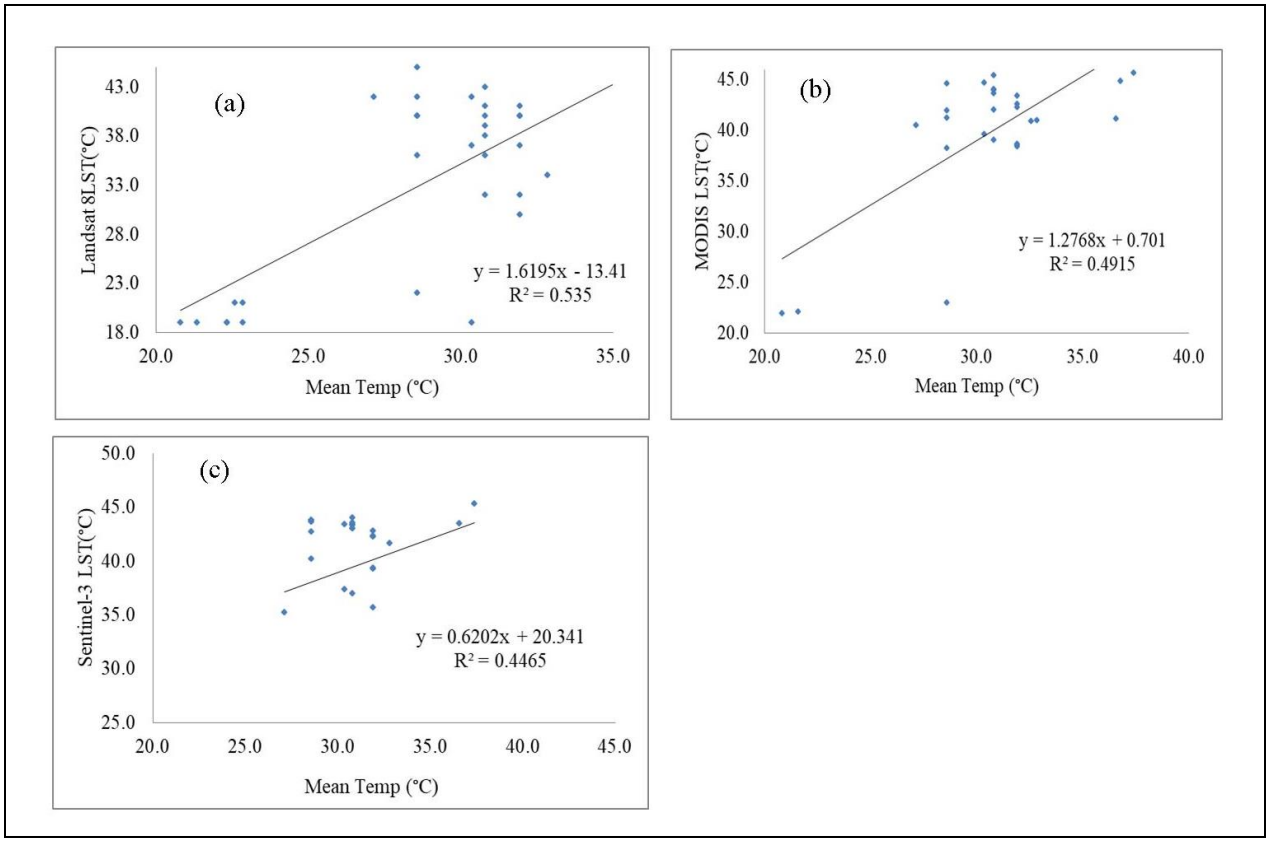

Figure 4.26 Relationship between Landsat 8 (a), MODIS (b) and Sentinel-3(c) driven LST vs. mean temperature in March.

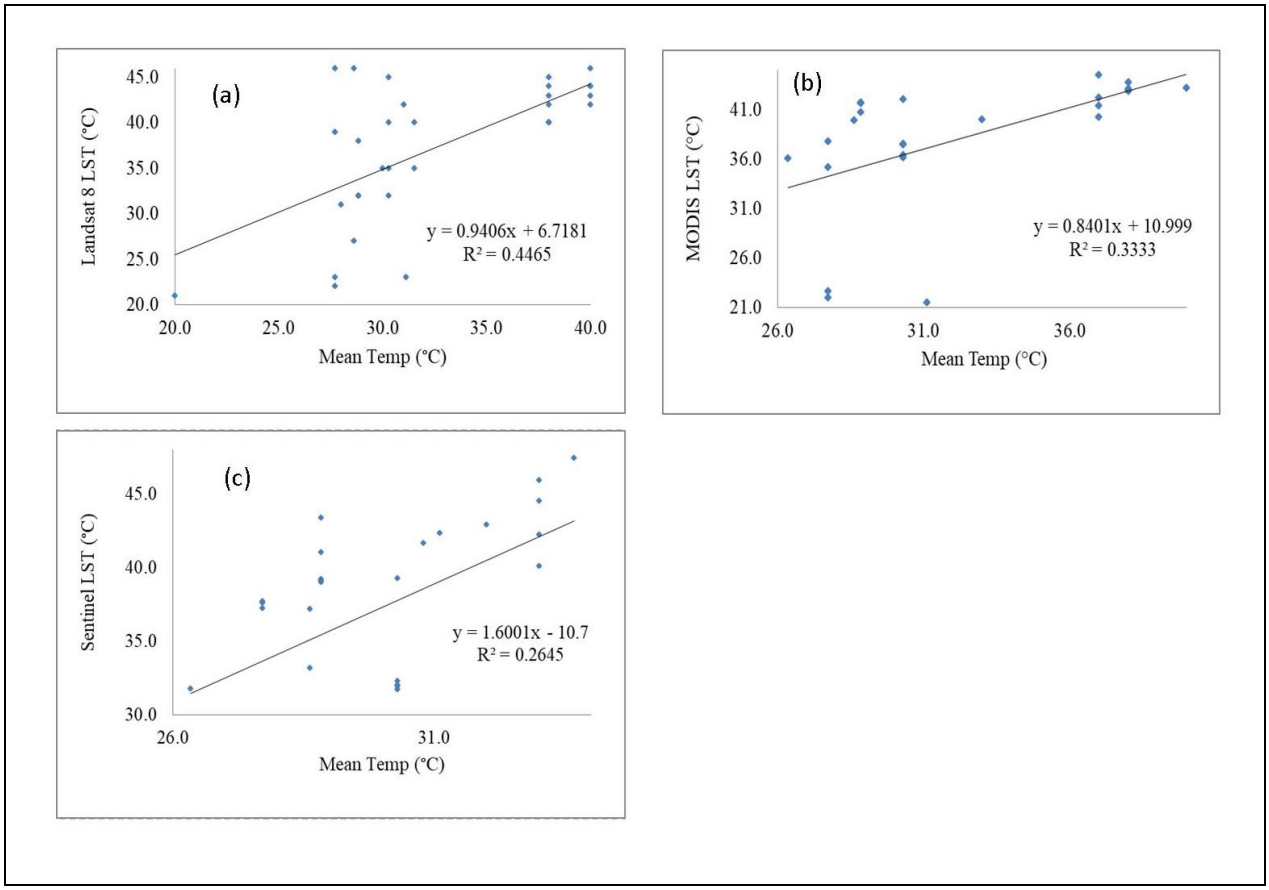

Figure 4.27 Relationship between Landsat 8 (a), MODIS (b) and Sentinel-3(c) driven LST vs mean temperature in April.

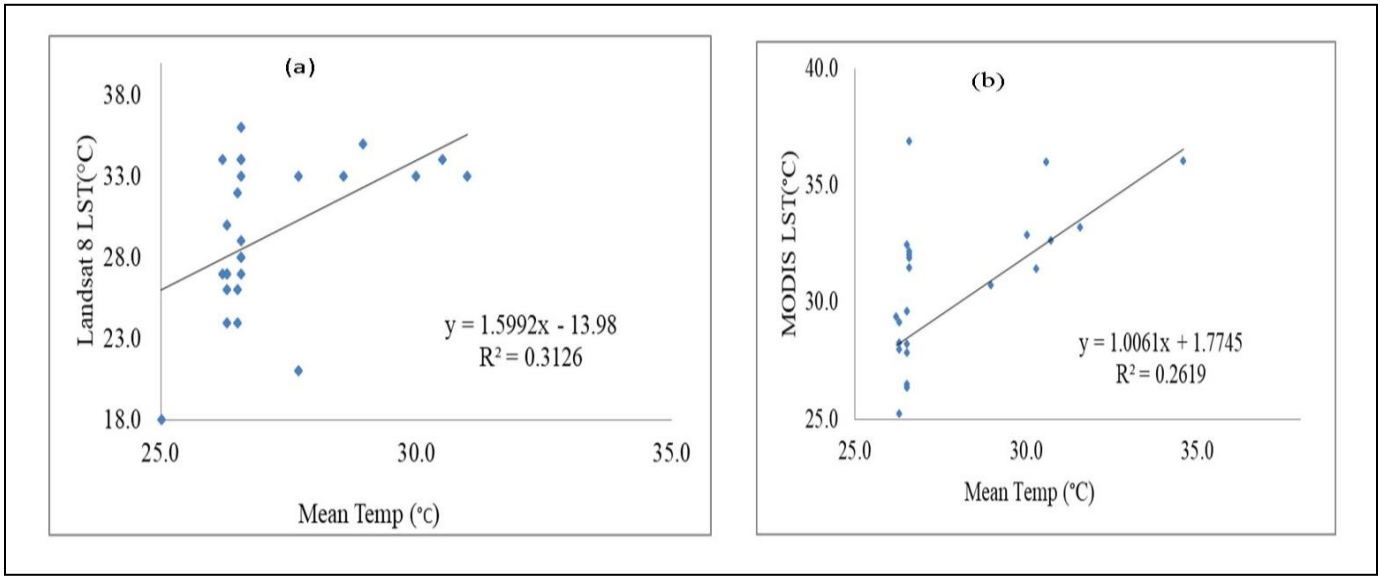

Figure 4.28 Relationship between Landsat 8 (a), MODIS (b) and Sentinel-3(c) driven LST vs mean temperature in June.

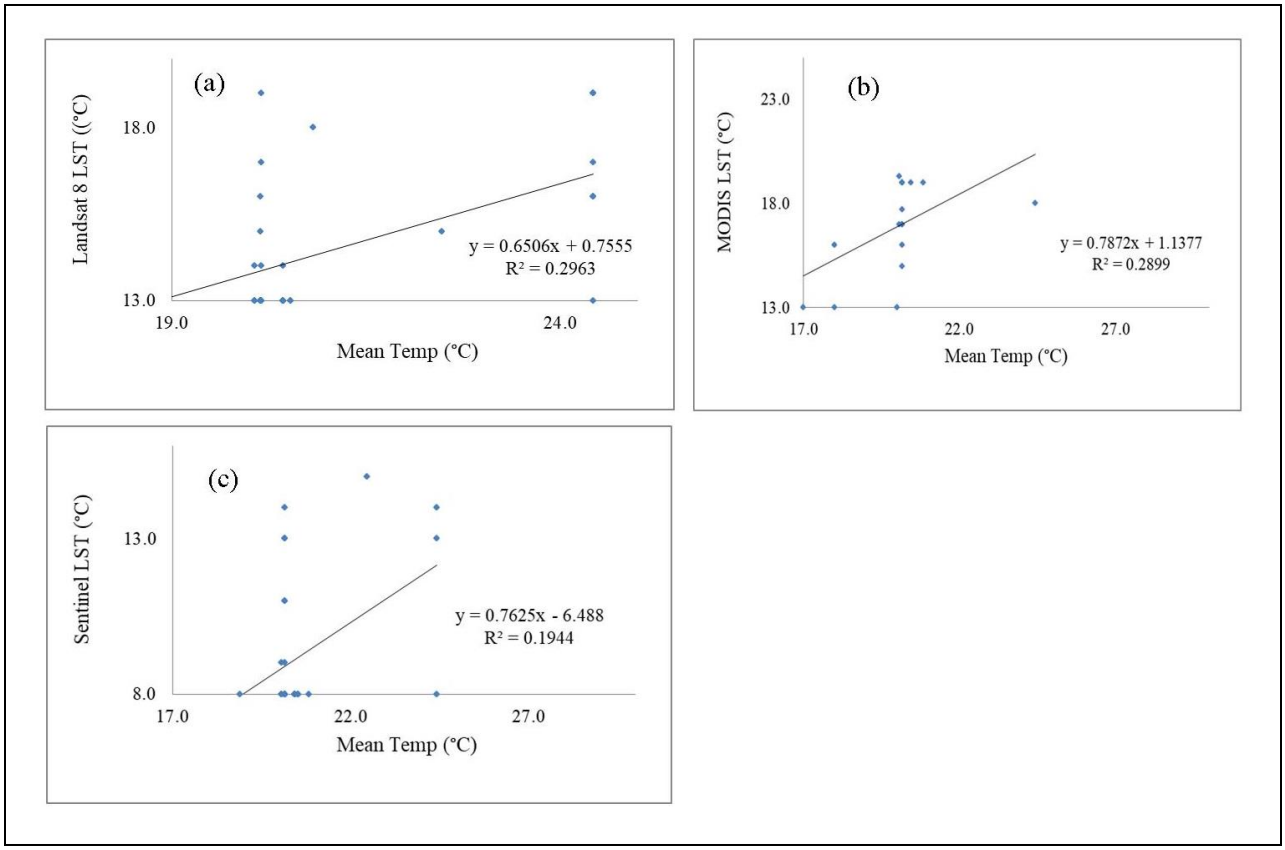

Figure 4.29 Relationship between Landsat 8 (a), MODIS (b) and Sentinel-3(c) driven LST vs. mean temperature in July.

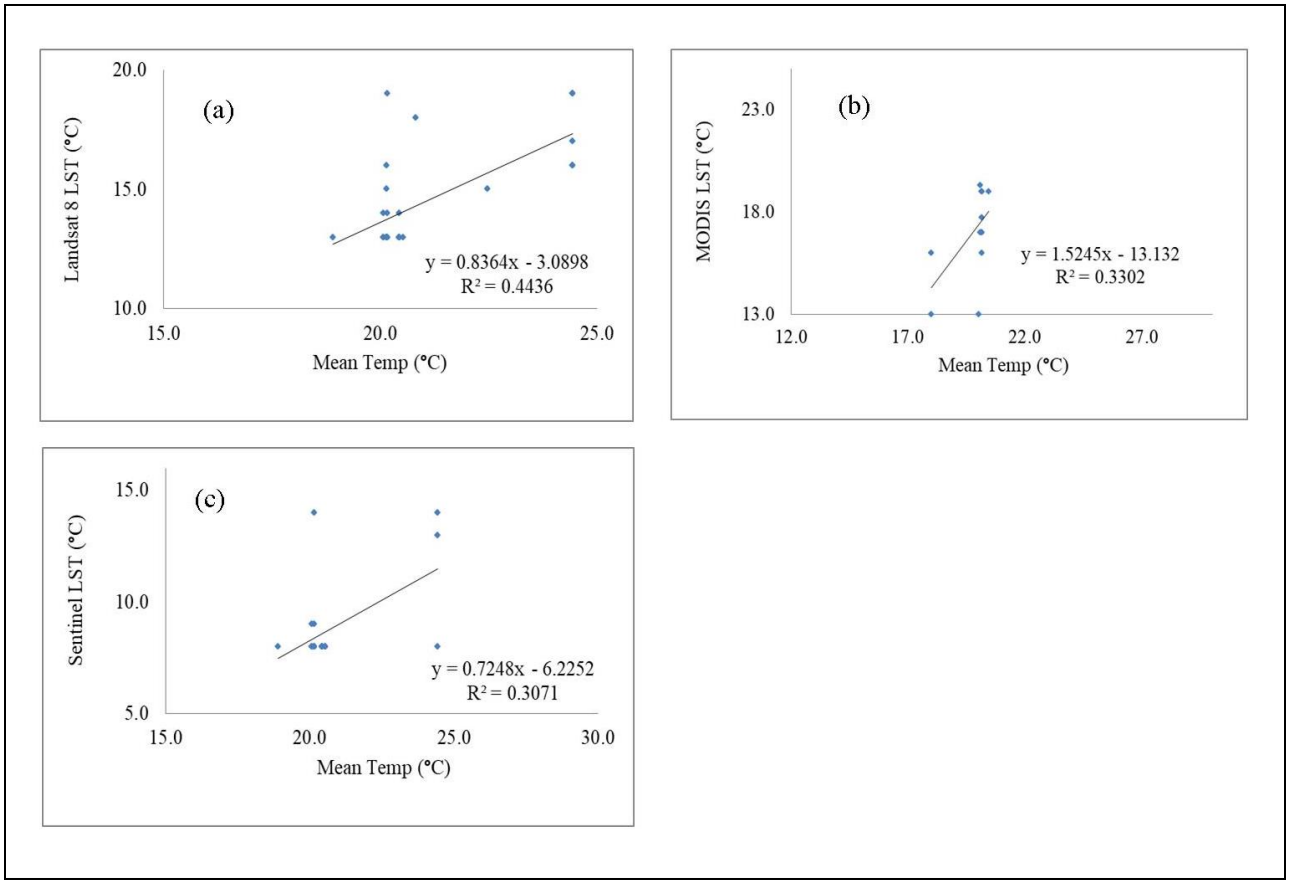

Figure 4. 30 Relationship between Landsat 8 (a), MODIS (b) and Sentinel-3(c) had driven LST vs mean temperature in August.

The Pearson correlation coefficient *r* was calculated in four months of the dry season and three months of wet (rainy) season (Table 4.10).

Table 4. 10 Pearson correlation coefficient r values of the different sensors.

Sensors	Months	Pearson r
Landsat 8	January	0.7
MODIS	January	0.52
Sentinel-3	January	0.56
Landsat 8	February	0.55
MODIS	February	0.51
Sentinel-3	February	0.52
Landsat 8	March	0.73
MODIS	March	0.7
Sentinel-3	March	0.52
Landsat 8	April	0.66
MODIS	April	0.58
Sentinel-3	April	0.51
Landsat 8	June	0.56
MODIS	June	0.51
Landsat 8	July	0.54
MODIS	July	0.53
Sentinel-3	July	0.44
Landsat 8	August	0.66
MODIS	August	0.57
Sentinel-3	August	0.55

CHAPTER FIVE

5. Discussion

5.1 NDVI

The NDVI results reveal that in January the highest mean value during the dry season. This leads to low LST in January which is in agreement with (Deng et al., 2018). Whereas in wet (rainy) the highest mean NDVI value was observed in August with 0.33. In all the months' the lowest NDVI value was observed in the central part of the study area.

5.2 LSE

The mean LSE ranges from 0.979 to 0.999 in the dry season. Similarly, in wet (rainy) season the LSE ranges from 0.974 to 0.997. The lowest LSE was observed in Lake Tana of the study area, this could be due to the presence of the lowest NDVI.

5.3 Land surface temperature

The main purpose of this research was to evaluate the LST in two different seasons of the year 2021 of Landsat 8, MODIS and Sentinel-3 over studied area.

As stated in chapter four the maximum LST was gained from Sentinel-3 in April with LST 51°C (Fig 4.14 c), whereas the minimum LST was 5 °C (Fig 4.12 a) from Landsat 8 during February of the dry season. Similarly, the maximum LST in wet (rainy) was extracted from Landsat 8 in June with 42°C (Fig 4.15 a) and the minimum was observed in Sentinel -3 in July with 8°C (Fig 4.16 c). According to (Getachew Bayable and Getnet Alemu, 2021) the dry season and wet (rainy) Min, Max and mean LST is in good agreement with previously conducted research in Amhara Region from 2001 to 2020. But there was a slight difference. This could be due to this research being conducted within the limited area of the Amhara Region and the minimum result is obtained from another sensor. So in general LST result is in good agreement with a similar study conducted in this region by Getachew Bayable and Getnet Alemu (2021).

5.4 Spatial and inter-seasonal variability's of LST

In this study, LST was varied Spatial inter-seasonally for different sensors. From Table 4.3 the maximum temperature was observed from sentinel-3 in April. Whereas, the minimum temperature was observed from sentinel-3 in July. In general, spatially the maximum LST

was observed in the periphery of the study area. Even though the minimum LST was observed in some parts of the periphery, mostly the minimum LST was observed in central parts of the study area. This is due to the presence of Lake Tana. The results of this study demonstrated that there was seasonal LST change that had been acquired even within a similar sensor. The results are supported by the research findings and conclusions of several previous studies (Ayanlade, 2016; Tarawally et al. 2021). The LST in wet (rainy) was low whereas high in the dry season. This is because the season was rainy and cloud effect. In the present study, cloud cover is a challenge with MODIS and Landsat 8, resulting in areas with no data, during the wet (rainy) season. Previous studies have reported similar results in another part of the world (Ayanlade, 2016).

From the Mann-Kendall trend test for both Landsat 8 and MODIS LST, there was a statistically insignificant increasing trend, whereas for Sentinel-3 no trend in the dry season. While, in wet (rainy) the Mann-Kendall trend tests for both Landsat 8 and MODIS LST, there was a statistically insignificant decreasing trend. In contrast Sentinel-3 mean LST revealed statistically insignificant decreasing trend.

5.5 Correlations of LST with mean near surface air temperature data

The relationship between temperature and results obtained from Landsat 8, MODIS and Sentinel-3 show strong values of r >= 0.5 in dry season and wet (rainy) (Table 4.4.). But there was a Pearson correlation coefficient r < 0.5 in July of sentinel-3. Landsat 8 was more correlated with mean temperature data over both dry season and wet (rainy) seasons. The highest r was calculated between Landsat 8 LST and mean temperature in March with 0.73 and again followed by Landsat 8 in January with r = 0.7 and MODIS of March with r= 0.7. During wet (rainy) the maximum correlation was observed in Landsat 8 of August with r=0.66 followed by MODIS with r=0.57. Therefore it can be said that, Landsat 8 LST had a better fit with mean near surface air temperature over the two sensors LST during two seasons.

The result showed that there was a high correlation between LST and mean near surface air temperature in dry season than wet (rainy). In contrast anther studies in else parts of the world showed that there was more correlation in wet (rainy) than dry season months (P.

Sheik Mujabar, 2019). This could be due to the season difference between Ethiopia and abroad.

CHAPTER SIX

6. Conclusion and Recommendations

6.1 Conclusion

The NDVI and LSE value lies between -0.61 to 0.70 and 0.974 to 0.999 in the study area over both seasons, respectively. This study evaluated the LST from three satellite images during different seasons. From the result, the minimum and maximum LST in the study area are varied both spatially and seasonally in Landsat 8, MODIS and Sentinel-3. The maximum LST was gained from Sentinel-3 in April with LST 51°C, whereas the minimum LST was 5 °C from Landsat 8 during February of the dry season. Similarly, the maximum LST in wet (rainy) was extracted from Landsat 8 in June with LST 42°C and the minimum was observed in Sentinel -3 in July with 8°C. Spatially, the maximum LST was observed in the periphery of the study area. Even though the minimum LST was observed in some parts of the periphery, the most minimum LST was observed in central parts of the study area. This is due to the presence of Lake Tana in the center. The relationship between mean temperature and LST obtained from Landsat 8, MODIS and Sentinel-3 shows strong values of r >= 0.5 in dry and wet (rainy) season, except July of Sentinel-3. The correlation result shows a better fit between temperature and LST results obtained from Landsat 8 followed by MODIS in the dry season. Similarly, Landsat 8 has a better correlation followed by MODIS in wet (rainy). In general, LST retrieved from Landsat 8 thermal bands shows better than the other two sensors in the study area. From the Mann-Kendall trend test for both Landsat 8 and MODIS LST, there was a statistically insignificant increase, whereas for Sentinel-3 no trend in the dry season. While, in wet (rainy) the Mann-Kendall trend tests for both Landsat 8 and MODIS LST, there was a statistically insignificant decreasing trend. In contrast Sentinel-3 mean LST revealed statistically insignificant decreasing trend.

6.2 Recommendations

Based on the results and conclusions drawn, the following recommendations are forwarded:

- ✓ The results of this study showed that LST derived from Landsat 8 is highly correlated with near-surface air temperature compared with MODIS and Sentinel-3

LST in Tana sub basin. Hence it is recommended that LST retrieved from Landsat 8 sensor is the most reliable.

- ✓ The study results indicated that satellite based retrieved LST is efficient in saving time and cost. Therefore, it is recommended to be used with caution.
- ✓ The result of this study was analyzed and interpreted with the focus of LST obtained mainly during the dry and wet (rainy) season of only one year. Therefore it is highly recommended that further researchers need to include all seasons.

References

Abebe Arega Mekonen and Arega Bazezew Berlie; (2020). Spatiotemporal variability trends of rainfall temperature in the Northeastern Highly of Ethiopia. *Modeling Earth Systems Environment*, *6*(1), 285–300.

Abrams, M., Hook, S., and Ramachran, B. (2002). ASTER user hbook, version 2. *Jet Propulsion Laboratory, 4800*, 135.

Ahmad, I., Tang, D., Wang, T., Wang, M., and Wagan, B. (2015). Precipitation trends over time using Mann-Kendall spearman's rho tests in a swat river basin, Pakistan. *Advances in Meteorology*, *2015*.

Albright, T. P., Pidgeon, A. M., Rittenhouse, C. D., Clayton, M. K., Flather, C. H., Culbert, P. D., and Radeloff, V. C. (2011). Heatwaves measured with MODIS l surface temperature data predict changes in avian community structure. *Remote Sensing of Environment*, *115*(1), 245–254.

Alkhaier, F., Flerchinger, G. N., and Su, Z. (2012). Shallow groundwater effect on l surface temperature surface energy balance under bare soil conditions: modeling description. *Hydrology Earth System Sciences*, *16*(7), 1817–1831.

Alemayehu Muluneh, Emiel van Loon, Woldeamlak Bewket, Saskia Keesstra, Leo Stroosnijder, and Ashenafi Burka; (2017). Effects of long-term deforestation remnant forests on rainfall temperature in the Central Rift Valley of Ethiopia. *Forest Ecosystems*, *4*(1), 1–17.

Anababu, D., Purushothaman, B. M., and Suresh, B. S. (2018). Estimation of l surface temperature using Landsat 8 data. *International Journal of Advance Research*, *4*(2), 177–186.

Aerson, M. C., Norman, J. M., Kustas, W. P., Houborg, R., Starks, P. J., and Agam, N. (2008). A thermal-based remote sensing technique for routine mapping of l-surface carbon, water energy fluxes from field to regional scales. *Remote Sensing of Environment*, *112*(12), 4227–4241.

Arnfield, A. J. (2003). Two decades of urban climate research: a review of turbulence,

exchanges of energy water, the urban heat isl. *International Journal of Climatology: A Journal of the Royal Meteorological Society*, *23*(1), 1–26.

Ayanlade, A. (2016). Variation in diurnal seasonal urban l surface temperature: luse change impacts assessment over Lagos metropolitan city. *Modeling Earth Systems Environment*, *2*(4), 1–8.

Barsi, J. A., Barker, J. L., and Schott, J. R. (2003). An atmospheric correction parameter calculator for a single thermal b earth-sensing instrument. *IGARSS 2003. 2003 IEEE International Geoscience Remote Sensing Symposium. Proceedings (IEEE Cat. No. 03CH37477)*, *5*, 3014–3016.

Bastiaanssen, W. G. M., Menenti, M., Feddes, R. A., and Holtslag, A. A. M. (1998). A remote sensing surface energy balance algorithm for l (SEBAL). 1. Formulation. *Journal of Hydrology*, *212*, 198–212.

Bateni, S. M., Entekhabi, D., and Jeng, D. S. (2013). Variational assimilation of l surface temperature the estimation of surface energy balance components. *Journal of Hydrology*, *481*, 143–156. https://doi.org/10.1016/j.jhydrol.2012.12.039

Becker, F., and Li, Z.-L. (1990). Temperature-independent spectral indices in thermal infrared bs. *Remote Sensing of Environment*, *32*(1), 17–33.

Begum, M. A. R. M. (2006). Application Of Non-Parametrictest For Trend Detection of Rainfall In The Largest Isl of Bangladesh. *ARPN J. Earth Sci.*, *2*, 40–44.

Brunsell, N. A., and Gillies, R. R. (2003). Length scale analysis of surface energy fluxes derived from remote sensing. *Journal of Hydrometeorology*, *4*(6), 1212–1219.

Center,L. P. D. A. A. (n.d.). No Title,. *MODIS Overview*. https://lpdaac.usgs.gov/lpdaac/products/modis_overview.

Chavez Jr, P. S. (1988). An improved dark-object subtraction technique for atmospheric scattering correction of multispectral data. *Remote Sensing of Environment*, *24*(3), 459–479.

Coll, C., Caselles, V., Sobrino, J. A., and Valor, E. (1994). On the atmospheric dependence of the split-window equation for l surface temperature. *Remote Sensing*, *15*(1), 105–

122.

Copernicus. (n.d.). *No Title*. https://www.copernicus.eu/en

Dash, P., Göttsche, F. M., Olesen, F. S., and Fischer, H. (2002). L surface temperature emissivity estimation from passive sensor data: Theory practice-current trends. *International Journal of Remote Sensing*, *23*(13). https://doi.org/10.1080/01431160110115041.

Duan, S.-B., Li, Z.-L., Cheng, J., and Leng, P. (2017). Cross-satellite comparison of operational l surface temperature products derived from MODIS ASTER data over bare soil surfaces. *ISPRS Journal of Photogrammetry Remote Sensing*, *126*, 1–10.

Filgueiras, R., Mantovani, E. C., Althoff, D., Dias, S. H. B., and Cunha, F. F. da. (2019). Sensitivity of evapotranspiration estimated by orbital images under influence of surface temperature. *Engenharia Agrícola*, *39*, 23–32.

Flynn, L. P., Harris, A. J. L., and Wright, R. (2001). Improved identification of volcanic features using Lsat 7 ETM+. *Remote Sensing of Environment*, *78*(1–2), 180–193.

Getachew Bayable and Getnet Alemu; (2021). Spatiotemporal variability of l surface temperature in north-western Ethiopia. *Environmental Science Pollution Research*, 1–13.

Hain, C. R., and erson, M. C. (2017). Estimating morning change in l surface temperature from MODIS day/night observations: Applications for surface energy balance modeling. *Geophysical Research Letters*, *44*(19), 9723–9733. https://doi.org/10.1002/2017GL074952

Hansen, J., Ruedy, R., Sato, M., and Lo, K. (2010). Global surface temperature change. *Reviews of Geophysics*, *48*(4).

Hu, X., Ren, H., Tansey, K., Zheng, Y., Ghent, D., Liu, X., and Yan, L. (2019). Agricultural drought monitoring using European Space Agency Sentinel 3A l surface temperature normalized difference vegetation index imageries. *Agricultural Forest Meteorology*, *279*, 107707.

Hulley, G. C., Hughes, C. G., and Hook, S. J. (2012). Quantifying uncertainties in l surface

temperature emissivity retrievals from ASTER MODIS thermal infrared data. *Journal of Geophysical Research: Atmospheres*, *117*(D23).

Irons, J. R., Dwyer, J. L., and Barsi, J. A. (2012). The next Lsat satellite: The Lsat data continuity mission. *Remote Sensing of Environment*, *122*, 11–21.

Jiménez-Muñoz, J. C., Cristóbal, J., Sobrino, J. A., Sòria, G., Ninyerola, M., and Pons, X. (2008). Revision of the single-channel algorithm for l surface temperature retrieval from Lsat thermal-infrared data. *IEEE Transactions on Geoscience Remote Sensing*, *47*(1), 339–349.

Jiménez-Muñoz, J. C., Sobrino, J. A., Skoković, D., Mattar, C., and Cristóbal, J. (2014). L surface temperature retrieval methods from Lsat-8 thermal infrared sensor data. *IEEE Geoscience Remote Sensing Letters*, *11*(10), 1840–1843.

Jiménez-Muñoz, J. C., and Sobrino, J. A. (2003). A generalized single-channel method for retrieving l surface temperature from remote sensing data. *Journal of Geophysical Research: Atmospheres*, *108*(D22).

Jin, M., and Dickinson, R. E. (2002). New observational evidence for global warming from the satellite. *Geophysical Research Letters*, *29*(10), 31–39.

Jin, M. S. (2012). Developing an index to measure urban heat isl effect using satellite l skin temperature l cover observations. *Journal of Climate*, *25*(18), 6193–6201.

Kalma, J. D., McVicar, T. R., and McCabe, M. F. (2008). Estimating l surface evaporation: A review of methods using remotely sensed surface temperature data. *Surveys in Geophysics*, *29*(4), 421–469.

Karnieli, A., Agam, N., Pinker, R. T., erson, M., Imhoff, M. L., Gutman, G. G., Panov, N., and Goldberg, A. (2010). Use of NDVI l surface temperature for drought assessment: Merits limitations. *Journal of Climate*, *23*(3), 618–633.

Khorchani, M., Martin-Hernez, N., Vicente-Serrano, S. M., Azorin-Molina, C., Garcia, M., Domínguez-Duran, M. [a]. A., Reig, F., Peña-Gallardo, M., and Domínguez-Castro, F. (2018). Average annual seasonal l surface temperature, spanish peninsular. *Journal of Maps*, *14*(2), 465–475. https://doi.org/10.1080/17445647.2018.1500316

Kogan, F. N. (2001). Operational space technology for global vegetation assessment. *Bulletin of the American Meteorological Society*, *82*(9), 1949–1964.

Kustas, W., and erson, M. (2009). Advances in thermal infrared remote sensing for l surface modeling. *Agricultural Forest Meteorology*, *149*(12), 2071–2081.

Lsat-missions. (n.d.). *Using the USGS Lsat Level-1 Data Product*. https://www.usgs.gov/lsat-missions/using-usgs-lsat-level-1-data-product

Li, Z.-L., Tang, B.-H., Wu, H., Ren, H., Yan, G., Wan, Z., Trigo, I. F., and Sobrino, J. A. (2013). Satellite-derived l surface temperature: Current status perspectives. *Remote Sensing of Environment*, *131*, 14–37.

Liu, F., Wang, X., Xu, J., and Gao, S. (2012). Sensitivity analysis of retrieving l surface emissivity based on the NDVI threshold method. *Remote Sensing Information*, *27*(04), 3–12.

LST_LSE_Review_IJRS_2002. (n.d.).

Meng, C. L., Li, Z. L., Zhan, X., Shi, J. C., and Liu, C. Y. (2009). L surface temperature data assimilation its impact on evapotranspiration estimates from the common l model. *Water Resources Research*, *45*(2), 1–14. https://doi.org/10.1029/2008WR006971

Mujabar, P. S. (2019). Spatial-temporal variation of l surface temperature of Jubail Industrial City, Saudi Arabia due to seasonal effect by using Thermal Infrared Remote Sensor (TIRS) satellite data. *Journal of African Earth Sciences*, *155*, 54–63.

Neway Kifle and Binyam Tesfaw; (2021). *MAPPING EFFECTS OF URBAN BLUE-GREEN LANDSCAPES ON L SURFACE TEMPERATURE USING GEO-SPATIAL TECHNIQUES: THE CASE OF ADDIS ABABA, ETHIOPIA.*

Njoku, E. G., Barnett, T. P., Laurs, R. M., and Vastano, A. C. (1985). Advances in satellite sea surface temperature measurement oceanographic applications. *Journal of Geophysical Research: Oceans*, *90*(C6), 11573–11586.

Norman, J. M., and Becker, F. (1995). Terminology in thermal infrared remote sensing of natural surfaces. *Agricultural Forest Meteorology*, *77*(3–4), 153–166.

Park, S., Kang, D., Yoo, C., Im, J., and Lee, M.-I. (2020). Recent ENSO influence on East

African drought during rainy seasons through the synergistic use of satellite reanalysis data. *ISPRS Journal of Photogrammetry Remote Sensing*, *162*, 17–26.

power data-access-viewer. (n.d.). https://power.larc.nasa.gov/data-access-viewer/

Prata, A. J., Caselles, V., Coll, C., Sobrino, J. A., and Ottle, C. (1995). Thermal remote sensing of l surface temperature from satellites: Current status future prospects. *Remote Sensing Reviews*, *12*(3–4), 175–224.

Qin, Q., Zhang, N., Nan, P., and Chai, L. (2011). Geothermal area detection using Lsat ETM+ thermal infrared data its mechanistic analysis—A case study in Tengchong, China. *International Journal of Applied Earth Observation Geoinformation*, *13*(4), 552–559.

Qin, Z., Karnieli, A., and Berliner, P. (2001). A mono-window algorithm for retrieving l surface temperature from Lsat TM data its application to the Israel-Egypt border region. *International Journal of Remote Sensing*, *22*(18), 3719–3746.

Quattrochi, D. A., and Luvall, J. C. (1999). Thermal infrared remote sensing for analysis of landscape ecological processes: methods applications. *Landscape Ecology*, *14*(6), 577–598.

Quattrochi, D. A., and Luvall, J. C. (2004). *Thermal remote sensing in l surface processing*. CRC Press.

Rajeshwari, A., and Mani, N. D. (2014). Estimation of l surface temperature of Dindigul district using Landsat 8 data. *International Journal of Research in Engineering Technology*, *3*(5), 122–126.

Reddy, S. N., and Manikiam, B. (2017). L surface temperature retrieval from LSAT data using emissivity estimation. *International Journal of Applied Engineering Research*, *12*(20), 9679–9687.

Remedios, J., and Emsley, S. (2012). *Sentinel-3 optical products algorithm definition l surface temperature*.

Samsone Tsegaye Mekasha, K.VSuryabhagavan, and Tibebu Kassawmar; (2021). Geospatial modeling of forest cover dynamics impact on climate variability in Awi

Zone, Ethiopia. *Tropical Ecology*, 1–17.

Schmugge, T., Hook, S. J., and Coll, C. (1998). Recovering surface temperature emissivity from thermal infrared multispectral data. *Remote Sensing of Environment*, *65*(2), 121–131.

Schneider, P., Ghent, D., Corlett, G., Prata, F., and Remedios, J. (n.d.). *AATSR Validation: LST Validation Implementation Plan*.

Shimelis G. Setegn, Srinivasan, R., and Dargahi, B. (2008). Hydrological modeling in the Lake Tana Basin, Ethiopia using SWAT model. *The Open Hydrology Journal*, *2*(1).

Sensor, M., Product, P., Id, N., Date, R., Preparation, V., Temperature, L. S., Notice, T. P., Centre, M. P., and Management, E. S. A. M. (2017). *S3 Product Notice – SLSTR*. 1–8.

Snyder, W. C., and Wan, Z. (1998). BRDF models to predict spectral reflectance emissivity in the thermal infrared. *IEEE Transactions on Geoscience Remote Sensing*, *36*(1), 214–225.

Snyder, W. C., Wan, Z., Zhang, Y., and Feng, Y.-Z. (1998). Classification-based emissivity for l surface temperature measurement from space. *International Journal of Remote Sensing*, *19*(14), 2753–2774.

Sobrino, J. A., Jiménez-Muñoz, J. C., Zarco-Tejada, P. J., Sepulcre-Cantó, G., Miguel, E. de, Soria, G., Romaguera, M., Julien, Y., Cuenca, J., and Hidalgo, V. (2009). Thermal remote sensing from Airborne Hyperspectral Scanner data in the framework of the SPARC SEN2FLEX projects: an overview. *Hydrology Earth System Sciences*, *13*(11), 2031–2037.

Sobrino, J. A., and Raissouni, N. (2000). Toward remote sensing methods for l cover dynamic monitoring: Application to Morocco. *International Journal of Remote Sensing*, *21*(2), 353–366.

Solanky, V., Singh, S., and Katiyar, S. K. (2018). L surface temperature estimation using remote sensing data. In *Hydrologic Modeling* (pp. 343–351). Springer.

Srivastava, P. K., Han, D., Ramirez, M. R., and Islam, T. (2013). Machine Learning Techniques for Downscaling SMOS Satellite Soil Moisture Using MODIS L Surface Temperature for Hydrological Application. *Water Resources Management*, *27*(8), 3127–3144. https://doi.org/10.1007/s11269-013-0337-9

Su, Z. (2002). The Surface Energy Balance System (SEBS) for estimation of turbulent heat fluxes. *Hydrology Earth System Sciences*, *6*(1), 85–100.

Sun, D., and Pinker, R. T. (2003). Estimation of l surface temperature from a Geostationary Operational Environmental Satellite (GOES-8). *Journal of Geophysical Research: Atmospheres*, *108*(D11).

Tang, H., and Li, Z.-L. (2013). *Quantitative remote sensing in thermal infrared: theory applications*. Springer Science and Business Media.

Tarawally, M., Xu, W., Kursah, M. B., and Kamara, A. B. (2021). Intra-seasonal variations in urban l surface temperature in two cities in Sierra Leone: the challenge of using a single-date image to represent a whole season. *Spatial Information Research*, 1–11.

Team, S.-3. (2013). *Sentinel-3 User Hbook (GMES-S3OP-EOPG-TN-13-0001)*. Paris, France: European Space Agency (ESA). http://sentinels.uat.esaportal.eu/documents/247904/685236/Sentinel-3_User_Hbook

Tomlinson, C. J., Chapman, L., Thornes, J. E., and Baker, C. (2011). Remote sensing l surface temperature for meteorology climatology: A review. *Meteorological Applications*, *18*(3), 296–306.

Valor, E., and Caselles, V. (1996). Mapping l surface emissivity from NDVI: Application to European, African, South American areas. *Remote Sensing of Environment*, *57*(3), 167–184.

Vlassova, L., and Pérez Cabello, F. (2016). *L Surface Temperature (LST) estimated from Lsat images: applications in burnt areas tree-grass woodls (dehesas)*. Universidad de Zaragoza, Prensas de la Universidad.

Voogt, J. A., and Oke, T. R. (2003). Thermal remote sensing of urban climates. *Remote Sensing of Environment*, *86*(3), 370–384.

Wagesho, N., Goel, N. K., and Jain, M. K. (2013). Temporal spatial variability of annual seasonal rainfall over Ethiopia. *Hydrological Sciences Journal*, *58*(2), 354–373.

Wan, Z. (1999). MODIS l-surface temperature algorithm theoretical basis document (LST ATBD). *Institute for Computational Earth System Science, Santa Barbara*, *75*, 18.

Wan, Z. (2014). New refinements validation of the collection-6 MODIS l-surface temperature/emissivity product. *Remote Sensing of Environment*, *140*, 36–45.

Wan, Z., and Dozier, J. (1996). A generalized split-window algorithm for retrieving l-surface temperature from space. *IEEE Transactions on Geoscience Remote Sensing*, *34*(4), 892–905.

Weldegerima, T. M., Zeleke, T. T., Birhanu, B. S., Zaitchik, B. F., and Fetene, Z. A. (2018). Analysis of rainfall trends its relationship with SST signals in the Lake Tana Basin, Ethiopia. *Advances in Meteorology*, *2018*.

Weng, Q. (2009). Thermal infrared remote sensing for urban climate environmental studies: Methods, applications, trends. *ISPRS Journal of Photogrammetry Remote Sensing*, *64*(4), 335–344.

Weng, Q., Lu, D., and Schubring, J. (2004). Estimation of l surface temperature–vegetation abundance relationship for urban heat isl studies. *Remote Sensing of Environment*, *89*(4), 467–483.

Worku Nega, Biniyam Tesfaw Hailu, and Aramde Fetene; (2019). An assessment of the vegetation cover change impact on rainfall land surface temperature using remote sensing in a subtropical climate, Ethiopia. *Remote Sensing Applications: Society Environment*, *16*, 100266.

Wubneh Belete, Tesfahun G/Michael, Elias Sime, B. B. F. N. (2017). Climate of Lake Tana Basin. *Springer International Publishing Switzerl*, pp51-58.

Yang, J., Zhou, J., Göttsche, F.-M., Long, Z., Ma, J., and Luo, R. (2020). Investigation validation of algorithms for estimating l surface temperature from Sentinel-3 SLSTR data. *International Journal of Applied Earth Observation Geoinformation*, *91*, 102136.

Yin, C. L., Meng, F., and Yu, Q. R. (2020). Calculation of l surface emissivity retrieval of l

surface temperature based on a spectral mixing model. *Infrared Physics and Technology*, *108*, 103333.

Yoo, C., Im, J., Cho, D., Yokoya, N., Xia, J., and Bechtel, B. (2020). Estimation of all-weather 1 km MODIS l surface temperature for humid wet (rainy) days. *Remote Sensing*, *12*(9), 1–23. https://doi.org/10.3390/RS12091398

Yoo, C., Im, J., Park, S., and Quackenbush, L. J. (2018). Estimation of daily maximum-minimum air temperatures in urban landscapes using MODIS time-series satellite data. *ISPRS Journal of Photogrammetry Remote Sensing*, *137*, 149–162. https://doi.org/10.1016/j.isprsjprs.2018.01.018

Yoo, C., and Park, S. (2020). *Spatial Downscaling of MODIS L Surface Temperature : Recent Research Trends, Challenges, Future Directions*. *36*(4), 609–626.

Yoo, C., Park, S., Kim, Y., and Cho, D. (2019). Analysis of thermal environment by urban expansion using KOMPSAT Landsat 8: Sejong City. *Korean Journal of Remote Sensing*, *35*(6_4), 1403–1415.

Yosef Mengistu Darge, Biniyam Tesfaw Hailu, Amha Atnafu Muluneh, and Tesfaye Kidane; (2019). Detection of geothermal anomalies using Landsat 8 TIRS data in Tulu Moye geothermal prospect, Main Ethiopian Rift. *International Journal of Applied Earth Observation Geoinformation*, *74*, 16–26.

Zhang, R., Tian, J., Su, H., Sun, X., Chen, S., and Xia, J. (2008). Two improvements of an operational two-layer model for terrestrial surface heat flux retrieval. *Sensors*, *8*(10), 6165–6187.

Ziaul, S., and Pal, S. (2018). Analyzing control of respiratory particulate matter on L Surface Temperature in local climatic zones of English Bazar Municipality Surroundings. *Urban Climate*, *24*, 34–50.

Appendices

Appendix 1**:** Agro-climatic zone of the study area.

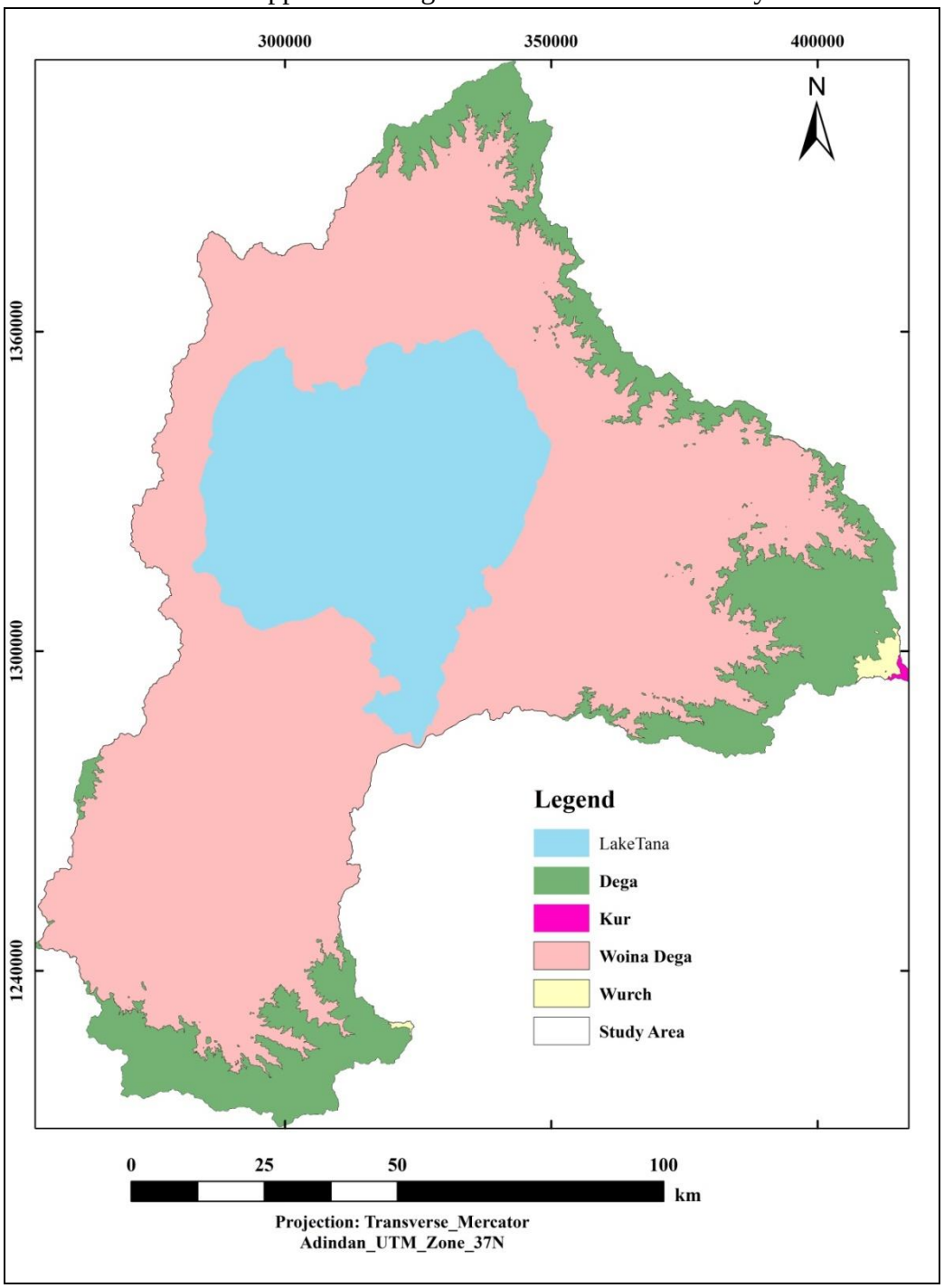

Appendix 2**:** False-color composite of January (a February (b, March (c and April (d dry season.

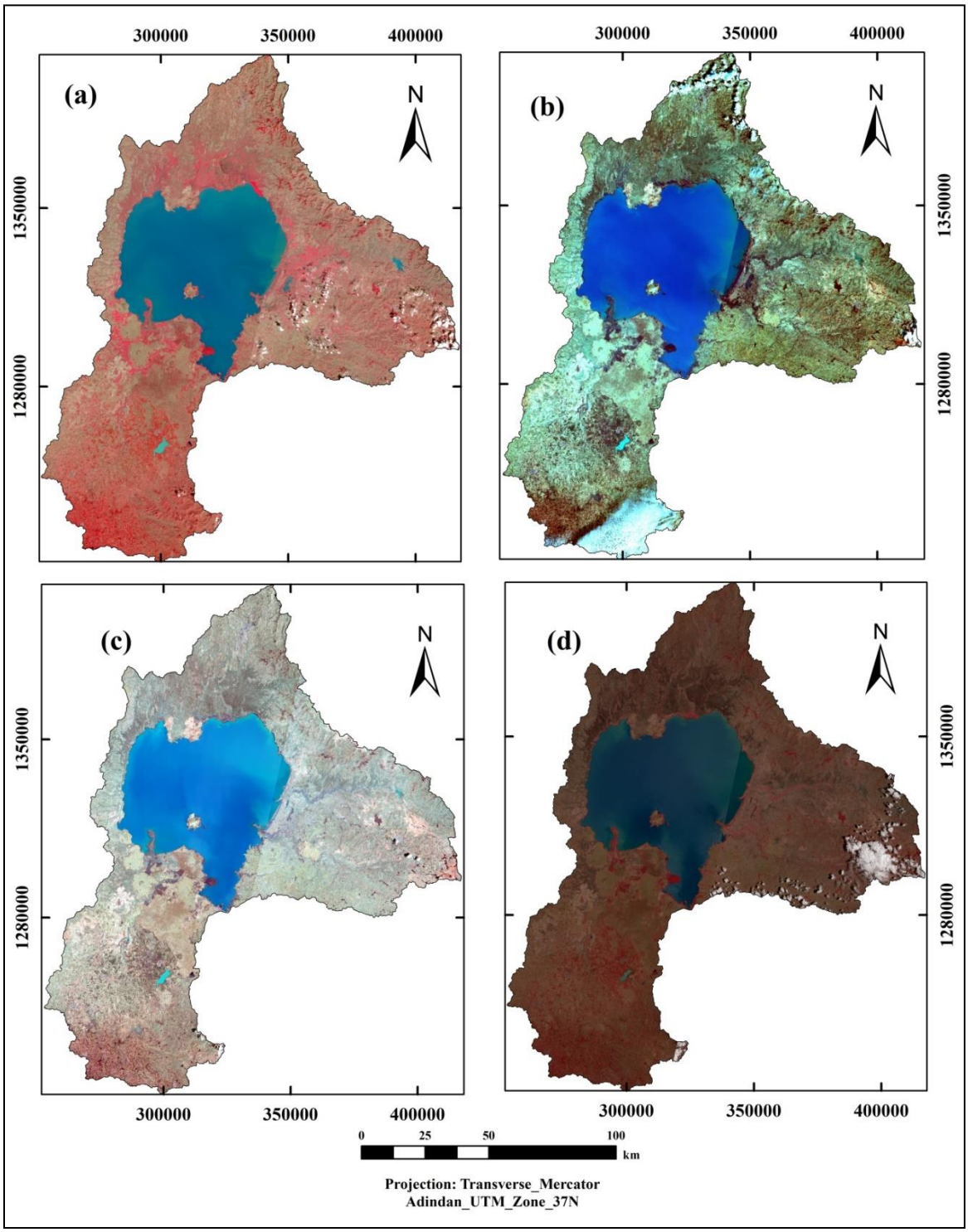

Appendix 3**:** Mean LSE of January (a February (b, March (c and April (d of the dry season**.**

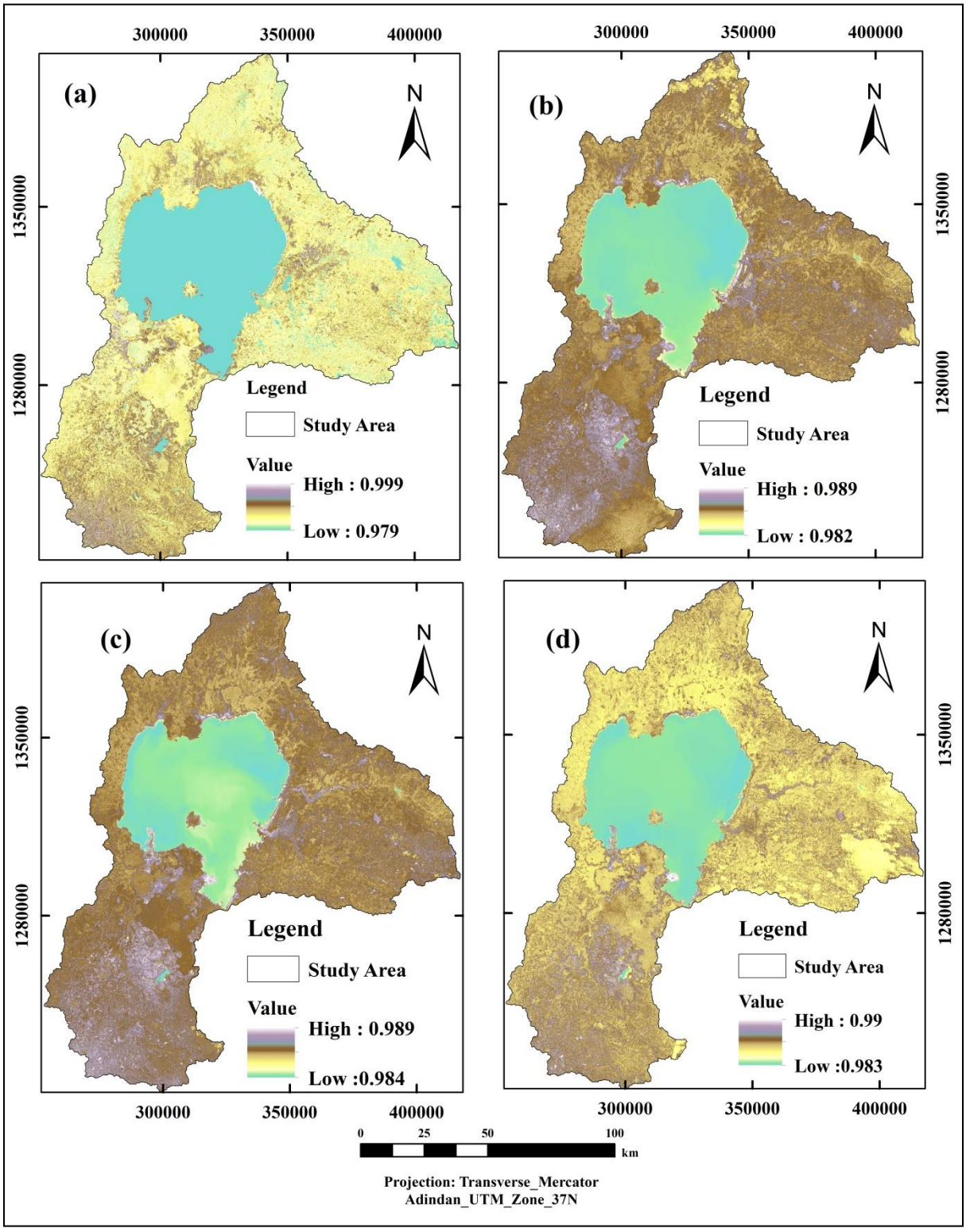

Appendix 4: Mean LSE of June (a July (b, and August (c of the wet (rainy) season.

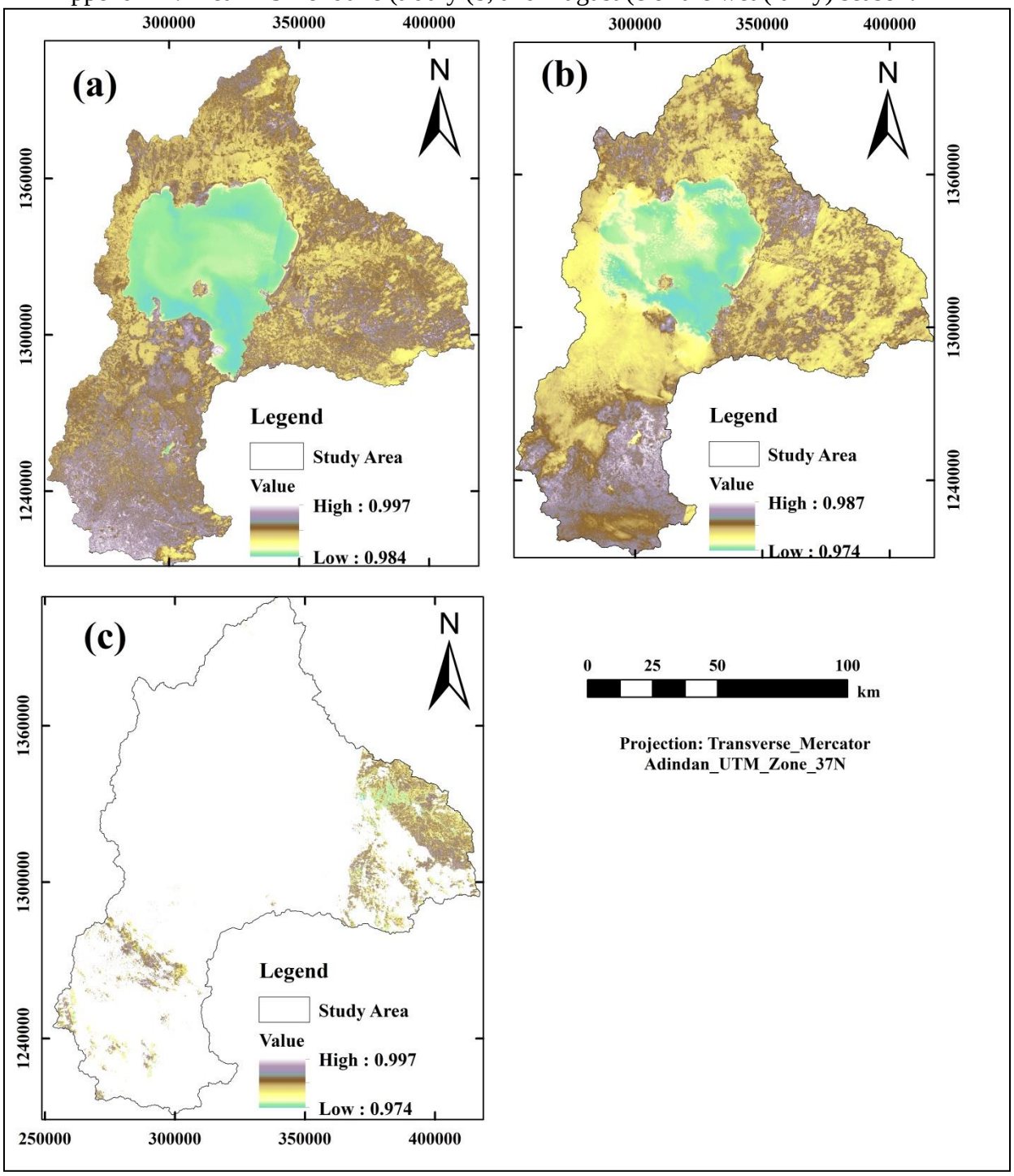

Appendix 5: March air temperature used for correlation